Monthly Notices of the ROYAL ASTRONOMICAL SOCIETY

MNRAS **524,** 4670–4687 (2023) https://doi.org/10.1093/mnras/stad2140
Advance Access publication 2023 July 17

Coronal properties of low-accreting AGNs using *Swift*, *XMM–Newton*, and *NuSTAR* observations

Arghajit Jana [1★] Arka Chatterjee [2★] Hsiang-Kuang Chang [1] Prantik Nandi [3] K. Rubinur [4,5] Neeraj Kumari [3] Sachindra Naik [3] Samar Safi-Harb[2] and Claudio Ricci [6,7]

[1]*Institute of Astronomy, National Tsing Hua University, Hsinchu 300044, Taiwan*
[2]*Department of Physics and Astronomy, University of Manitoba, Winnipeg, MB R3T 2N2, Canada*
[3]*Astronomy & Astrophysics Division, Physical Research Laboratory, Navrangpura, Ahmedabad, Gujarat 38009, India*
[4]*National Centre for Radio Astrophysics – Tata Institute of Fundamental Research (NCRA-TIFR), S. P. Pune University Campus, Ganeshkhind, Pune 411007, India*
[5]*Institute of Theoretical Astrophysics, University of Oslo, P.O box 1029 Blindern, 0315 OSLO, Norway*
[6]*Instituto de Estudios Astrofísicos, Facultad de Ingeniería y Ciencias, Universidad Diego Portales, Av. Ejército Libertador 441, Santiago, Chile*
[7]*Kavli Institute for Astronomy and Astrophysics, Peking University, Beijing 100871, People's Republic of China*

Accepted 2023 July 12. Received 2023 June 20; in original form 2022 October 28

ABSTRACT

We studied the broad-band X-ray spectra of *Swift*/Burst Alert Telescope selected low-accreting active galactic nuclei (AGNs) using the observations from *XMM–Newton*, *Swift*, and *NuSTAR* in the energy range of 0.5–150 keV. Our sample consists of 30 AGNs with Eddington ratio, $\lambda_{\rm Edd} < 10^{-3}$. We extracted several coronal parameters from the spectral modelling, such as the photon index, hot electron plasma temperature, cutoff energy, and optical depth. We tested whether there exist any correlation/anticorrelation among different spectral parameters. We observe that the relation of hot electron temperature with the cutoff energy in the low accretion domain is similar to what is observed in the high accretion domain. We did not observe any correlation between the Eddington ratio and the photon index. We studied the compactness–temperature diagram and found that the cooling process for extremely low-accreting AGNs is complex. The jet luminosity is calculated from the radio flux, and observed to be related to the bolometric luminosity as $L_{\rm jet} \propto L_{\rm bol}^{0.7}$, which is consistent with the standard radio-X-ray correlation.

Key words: accretion, accretion discs – black hole physics – galaxies: active – quasars: supermassive black holes – galaxies: Seyfert – X-rays: galaxies.

1 INTRODUCTION

Active galactic nuclei (AGNs) are powered by the accreting supermassive black holes (SMBHs) that reside at the centre of most galaxies (Rees 1984). The matter gets accreted on to the SMBH, where the gravitational potential energy is converted into radiation, which is emitted over the entire electromagnetic spectrum. The X-rays are thought to be produced in a hot electron cloud, known as the corona, located in the vicinity of the black hole (Haardt & Maraschi 1991; Narayan & Yi 1994; Chakrabarti & Titarchuk 1995; Done, Gierliński & Kubota 2007). The primary X-ray continuum is produced through the inverse-Comptonization (Sunyaev & Titarchuk 1980, 1985; Haardt & Maraschi 1991) of the seed UV photons from the standard accretion disc (Shakura & Sunyaev 1973). The X-ray continuum can be reprocessed by the accretion disc and/or the molecular torus, which produces a reflection hump at ∼15–40 keV and an iron Kα line at ∼6.4 keV (George & Fabian 1991; Matt, Perola & Piro 1991). Additionally, an excess in the soft X-ray energy band (<2 keV), known as soft-excess, is observed in several sources (Arnaud et al. 1985; Singh, Garmire & Nousek 1985). The origin of the soft-excess is still debated, and some of the possible explanations proposed include blurred reflection from the inner disc (Lohfink et al. 2012), a warm corona (Mehdipour et al. 2011; Done et al. 2012), or a small number of scattering in a hot corona (Nandi et al. 2021).

In general, an AGN is classified as a low-luminosity AGN (LLAGN), if the bolometric luminosity is $L_{\rm bol} < 10^{44}$ erg s^{-1} (e.g. Gu & Cao 2009). Recent studies have suggested that the mass-normalized accretion rate is the primary driver in the evolution of the circumnuclear gas in AGNs (e.g. Ricci et al. 2017a). It is believed that the accretion mechanism is different in the low-accreting AGNs (LAC-AGNs; Eddington ratio, $\lambda_{\rm Edd} = L_{\rm bol}/L_{\rm Edd} < 10^{-3}$, where $L_{\rm Edd}$ is Eddington luminosity) from the high-accreting AGNs (HAC-AGNs; $\lambda_{\rm Edd} > 10^{-3}$; e.g. Ho 2009; Yang et al. 2015; Kawamuro et al. 2016).

Theory predicts that if the accretion rate falls below a critical level, the inner accretion flow changes from the geometrically thin, optically thick accretion disc (Shakura & Sunyaev 1973) to an optically thin, radiatively inefficient accretion flow (Esin, McClintock & Narayan 1997). The correlation between the $\lambda_{\rm Edd}$ and photon index (Γ) could be considered as an observational manifestation of such a theoretical claim. While a positive correlation has been found for high-luminosity AGNs (e.g. Shemmer et al. 2006, 2008), an anticorrelation is observed for low-luminosity AGNs (e.g. Gu & Cao

★ E-mail: argha0004@gmail.com (AJ); arka.chatterjee@umanitoba.ca (AC)

2009; Ho 2009). It is, therefore, widely believed that in LLAGNs, the standard thin accretion disc is replaced by a radiatively inefficient accretion flow (e.g. Narayan et al. 1998; Quataert 2001; Ho 2009). The absence of the big-blue bump in the SED of these objects suggests that the thin accretion disc gets truncated at a large distance from the BH (e.g. Mason et al. 2012; Nemmen, Storchi-Bergmann & Eracleous 2014). Moreover, most LLAGNs do not show the broad iron K-line feature, suggesting that the standard disc does not get extended to the innermost region around the SMBH (e.g. Kawamuro et al. 2016; Younes et al. 2019).

In the case of the HAC-AGNs, the majority of the seed photons that produce the X-ray emission, are most likely thermal and originate in a standard accretion disc (e.g. Shakura & Sunyaev 1973; Malkan & Sargent 1982). However, for LAC-AGNs, the origin of the seed photons could be dominated by non-thermal processes, such as synchrotron emission occurring in the jet or within the corona (e.g. Yang et al. 2015). The size, shape, and geometry of the corona are highly debated. Various studies suggest that the X-ray corona is compact ($\sim$10 R_g, where R_g is gravitational radius; e.g. McHardy et al. 2005; Chartas et al. 2009; Risaliti et al. 2011; Reis & Miller 2013; Uttley et al. 2014) and located close to the black hole ($\sim$3–10 R_g; e.g. Fabian et al. 2009, 2015, 2017; Zoghbi et al. 2012; Kara et al. 2013). In the low-accreting AGNs ($L < 10^{-4} L_{\rm Edd}$, where $L_{\rm Edd}$ is the Eddington luminosity; e.g. Reis & Miller 2013), the hard X-rays could originate in a hot quasi-spherical accretion flow or in an extended corona ($\sim$100 R_g).

The corona in AGN is typically characterized by the electron plasma temperature ($kT_{\rm e}$) and optical depth ($\tau_{\rm e}$). The electron temperature is directly related to the cutoff energy ($E_{\rm cut}$), while the photon index is connected to both $kT_{\rm e}$ and $\tau_{\rm e}$ (e.g. Sunyaev & Titarchuk 1980; Pozdnyakov, Sobol & Syunyaev 1983; Petrucci et al. 2001). The photon index (Γ) and the high energy cutoff ($E_{\rm cut}$) can be inferred by X-ray spectroscopic analysis of AGN. The photon index has been studied over the past three decades. In contrast, the study of the high energy cutoff has been limited until more recent times due to the restricted bandpass of the X-ray facilities. Recently, the cutoff energy of the AGNs has been measured using various observatories with hard X-ray instruments, e.g. *BeppoSAX* (Perola et al. 2002; Dadina 2007), *INTEGRAL* (Molina et al. 2009, 2013; Panessa et al. 2011; de Rosa et al. 2012), *NuSTAR* (Kamraj et al. 2018, 2022; Rani, Stalin & Goswami 2019; Baloković et al. 2020) and *Swift* (Ricci et al. 2017a, 2018; Trakhtenbrot et al. 2017). In general, the cutoff energy is observed in a wide range of $\sim$50–500 keV (e.g. Ricci et al. 2017a, 2018; Baloković et al. 2020). Ricci et al. (2018) analyzed 838 Burst Alert Telescope (BAT) AGNs and found that the median of the cutoff energy, $E_{\rm cut} = 160 \pm 41$ keV for $L/L_{\rm Edd} > 0.1$, and $E_{\rm cut} = 370 \pm 51$ keV for $L/L_{\rm Edd} < 0.1$. They also found the median of the hot electron temperature and optical depth as $kT_{\rm e} = 105 \pm 18$ keV and $\tau_{\rm e} = 0.25 \pm 0.06$, respectively.

While the coronal properties of the HAC-AGNs have been explored extensively in past (e.g. Ricci et al. 2017a, 2018; Kamraj et al. 2018, 2022; Rani et al. 2019; Baloković et al. 2020; Hinkle & Mushotzky 2021), the low accretion domain has been considerably less explored (e.g. Younes et al. 2019). Several X-ray studies of LLAGNs have been performed to study the variation of the photon index (e.g. Shemmer et al. 2008; Gu & Cao 2009; Ho 2009; Kawamuro et al. 2016).

In this paper, we study the coronal properties of low-accreting AGNs using broad-band X-ray data obtained from *NuSTAR* and *Swift*/BAT in the 3–150 keV range. Using Comptonization models, we constrain the main coronal parameters and study possible trends among them. The paper is organized in the following way. First, in Section 2, we describe the sample selection and data reduction processes. Then, we discuss the analysis procedure in Section 3. Next, the results of our work are presented and discussed in Section 4. Finally, we summarize our findings in Section 5.

2 SAMPLE AND DATA REDUCTION

2.1 Sample selection

The primary aim of this work is to investigate the coronal properties of low-accreting AGNs. We chose our sample from the all-sky *Swift*/BAT hard X-ray survey[1] (Oh et al. 2018). The BAT survey was compiled for 105 months, and the spectra are stacked together. The survey has a sensitivity of 8.4×10^{-12} erg cm^{-2} s^{-1} in 14–195 keV range, and is almost unbiased by obscuration up to $N_{\rm H} \sim 10^{24}$ cm^{-2} (Ricci et al. 2015). Initially, we chose a sample of AGNs within the range of 14–195 keV, where the luminosity is less than 10^{45} erg s^{-1}. Our main goal is to select sources with an Eddington ratio $<10^{-3}$.

We selected all BAT AGNs with publicly available *NuSTAR* observations. We also added *XMM–Newton* or *Swift*/XRT observations for the soft X-ray band (0.5–10 keV) to construct the spectra in a broad energy range of 0.5–150 keV[2] From the combined spectra, we performed spectral analysis to calculate the bolometric luminosity ($L_{\rm bol}$) and Eddington ratio ($\lambda_{\rm Edd}$; see Section 3 for details). We selected sources with $\lambda_{\rm Edd} < 10^{-3}$ for our sample. We excluded several sources from our sample (with $\lambda_{\rm Edd} < 10^{-3}$) due to low signal-to-noise ratio (SNR), e.g. NCG 660, NGC 3486, NGC 678, or the presence of other sources in the field of view, e.g. NGC 5194. In the case of NGC 5194, several ULXs have been detected in the *NuSTAR* field. As *NuSTAR* does not resolve them, the emission is not purely from the AGN (Brightman et al. 2018). Hence, we did not include NGC 5194 in our sample. The final sample consists of 30 sources and is tabulated in Table 1. In Fig. 1, we show the distribution of Eddington ratio ($\lambda_{\rm Edd}$), black hole mass ($M_{\rm BH}$), and bolometric luminosity ($L_{\rm bol}$) of our sample, in the left-hand, middle, and right-hand panels, respectively. Our sample extends over three orders of magnitude for all three parameters.

2.2 Data reduction

2.2.1 *NuSTAR*

NuSTAR is a hard X-ray focusing telescope with two identical modules, FPMA and FPMB, and operates in the 3–78 keV energy range (Harrison et al. 2013). We obtained *NuSTAR* data from NASA's HEASARC archive.[3] The data were reprocessed with the *NuSTAR* Data Analysis Software (`NuSTARDAS`[4], version 1.4.1). We generated clean event files with the `nupipeline` task, using standard filtering criteria. The data were calibrated using the latest calibration data files available in the *NuSTAR* calibration data base.[5] The source and background products were extracted by considering circular regions with 60 arcsec, and 90 arcsec radii, centred at the source coordinates and away from the source, respectively. The spectra were

[1] https://swift.gsfc.nasa.gov/results/bs105mon/
[2] Check Appendix A for details.
[3] https://heasarc.gsfc.nasa.gov/cgi-bin/W3Browse/w3browse.pl
[4] https://heasarc.gsfc.nasa.gov/docs/nustar/analysis/
[5] http://heasarc.gsfc.nasa.gov/FTP/caldb/data/nustar/fpm/

Table 1. Information on the selected sources.

	Name	Swift name	Type	RA (J2000)	Dec. (J2000)	Redshift	log (M_{BH})	Ref.
(1)	NGC 454E	J0114.4–5522	Seyfert 2	18.575	–55.401	0.0121	8.52 ± 0.45	1
(2)	NGC 1052	J0241.3–0816	Seyfert 2	40.270	–8.256	0.005	8.96 ± 0.29	1
(3)	NGC 2110	J0552.2–0727	Seyfert 2	88.046	–7.457	0.007	9.38	2
(4)	NGC 2655	J0856.0+7812	Seyfert 2	133.90	78.20	0.0047	7.70 ± 0.20	3
(5)	NGC 3079	J1001.7+5543	Seyfert 2	150.49	55.679	0.0037	8.27 ± 0.30	1
(6)	NGC 3147	J1017.8+7340	Seyfert 2	155.45	73.41	0.0093	8.79	4
(7)	NGC 3718	J1132.7+5301	LINER 1.9	173.22	53.02	0.0033	9.53	1
(8)	NGC 3786	J1139.5–6526	Seyfert 1.9	174.94	31.96	0.0089	7.53	5
(9)	NGC 3998	J1157.8+5529	LINER 1.9	179.48	55.45	0.0035	9.93 ± 0.33	1
(10)	NGC 4102	J1206.2+5243	LINER	181.59	52.71	0.0028	8.75 ± 0.33	1
(11)	NGC 4258	J1219.4+4720	Seyfert 1.9/LINER	184.75	47.29	0.0015	7.57 ± 0.35	1
(12)	NGC 4579	J1237.5+1182	LINER 1.9	189.38	11.82	0.0051	8.10	6
(13)	NGC 5033	J1313.6+3650B	Seyfert 1.5	198.406	36.826	0.0029	7.86 ± 0.35	1
(14)	NGC 5283	J1341.5+6742	Seyfert 2	205.299	67.691	0.010	8.87 + 0.30	1
(15)	NGC 5290	J1345.5+4139	Seyfert 2	206.329	41.713	0.0080	7.76 ± 0.31	1
(16)	NGC 5899	J1515.0+4205	Seyfert 2	228.788	42.063	0.0080	8.66 ± 0.31	1
(17)	NGC 6232	J1643.2+7036	Seyfert 1	250.721	70.643	0.0148	7.43 ± 0.52	1
(18)	NGC 7213	J2209.4–4711	Seyfert 1	332.33	–47.17	0.0058	7.99	5
(19)	NGC 7674	J2328.1+0883	Seyfert 2	352.031	8.835	0.028	9.18	2
(20)	Mrk 18	J0902.0+6007	Seyfert 2	135.493	60.152	0.0111	7.85 ± 0.30	1
(21)	Mrk 273	J1344.7+5588	Seyfert 2	206.175	55.887	0.0379	9.02 ± 0.04	7
(22)	ARP 102B	J1719.7+4900	Seyfert 1	259.81	48.98	0.0242	8.92 ± 0.34	1
(23)	ESO 253–003	J0525.3−4600	Seyfert 2	81.381	–45.965	0.042	9.84	2
(24)	ESO 506–027	J1238.9–2720	Seyfert 2	189.722	–27.294	0.025	8.99 ± 0.29	1
(25)	HE 1136–2304	J1139.0–2323	Seyfert 1.9	74.713	–23.360	0.027	9.39	2
(26)	IGR J11366–6002	J1136.7+6738	Seyfert 1	174.104	67.645	0.014	8.56	2
(27)	IC 4518A	J1457.8–4308	Seyfert 2	224.460	–43.116	0.016	8.79	2
(28)	UGC 12 282	J2258.9+4054	Seyfert 1	344.696	40.918	0.017	9.80 ± 0.35	1
(29)	LEDA 214543	J1650.5+0434	Seyfert 2	252.656	4.620	0.032	9.83 ± 0.32	1
(30)	Z367–9	J1621.2+8104	Seyfert 2	244.927	81.062	0.027	9.82 ± 0.32	1

Note. (1) Koss et al. (2017), (2) Koss et al. (2022), (3) Tully (1988), (4) Merloni, Heinz & di Matteo (2003), (5) Woo & Urry (2002), (6) Younes et al. (2019), and (7) U et al. (2013).

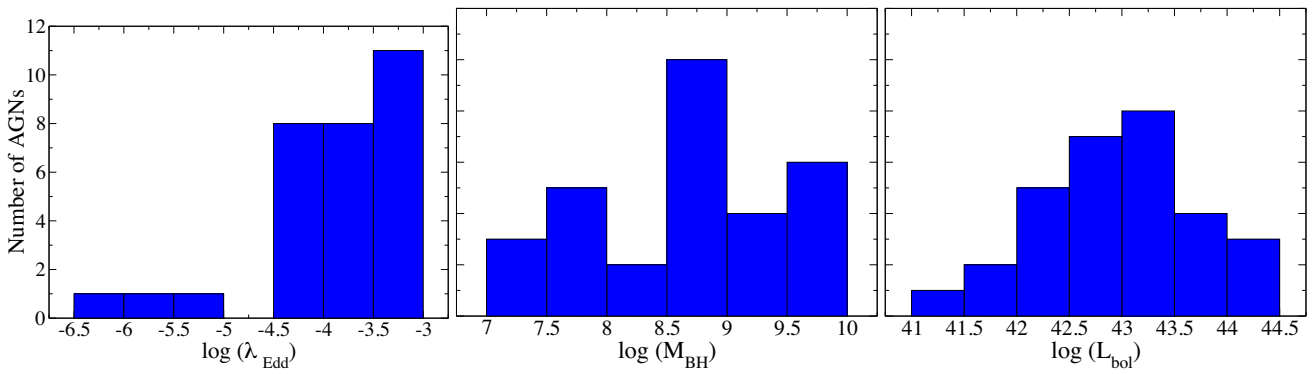

Figure 1. Histograms of Eddington ratio (λ_{Edd}), supermassive black hole mass (M_{BH}), and bolometric luminosity (L_{bol}) are shown in the left-hand, middle, and right-hand panels, respectively.

extracted using the `nuproduct` task and then rebinned to ensure that they had at least 20 counts per bin by using the `grppha` task. For each source, we used the *NuSTAR* observation with the longest exposure, except for NGC 3718 for which we co-added the spectra from four continuous observations to improve the SNR using the `FTOOL` task ADDASCASPEC.

2.3 Swift

The 0.5–8 keV *Swift*/XRT spectra were generated using the standard online tools provided by the UK Swift Science Data Centre (Evans et al. 2009).[6] We utilized the *Swift*/XRT spectra for 17 objects when the simultaneous observations were available with *NuSTAR*. For five objects, we stacked several XRT spectra together to achieve a good SNR.

The 14–150 keV *Swift*/BAT spectra and response matrices were obtained from the 105-month *Swift*-BAT All-sky Hard X-Ray Survey.[7]

[6] https://www.swift.ac.uk/user_objects/
[7] https://swift.gsfc.nasa.gov/results/bs105mon/

Table 2. Observation log.

Object	*NuSTAR* ID	Date (yyyy-dd-mm)	Exp (ks)	*XMM–Newton* or XRT ID	Date (yyyy-dd-mm)	Exp (ks)
NGC 454E	60061009002	2016-02-14	24	00 080 016 001	2016-02-14	6
NGC 1052	60061027002	2013-02-14	16	0790980101^{X*}	2017-01-17	71
NGC 2110	60061061002	2012-10-05	15	0145670101^{X*}	2003-03-05	60
NGC 2655	60160341004	2016-11-10	16	00081037001–02	2016-11-02 – 03	7
NGC 3079	60061097002	2013-11-12	22	00 080 030 001	2013-11-12	7
NGC 3147	60101032002	2015-12-27	49	0405020601^{X*}	2006-06-10	18
NGC 3718	60301031002	2017-10-24	25	0795730101^{X}	2017-10-24	38
	60301031004	2017-10-27	90			
	60301031006	2017-10-30	57			
	60301031008	2017-11-03	57			
NGC 3786	60061349002	2014-06-09	22	00 080 684 001	2014-06-09	4
NGC 3998	60201050002	2016-10-25	104	0790840101^{X}	2016-10-26	25
NGC 4102	60160472002	2015-11-19	21	00 081 110 001	2015-11-09	7
NGC 4258	60101046002	2015-11-16	55	00 081 700 001	2015-11-16	2
NGC 4579	60201051002	2016-12-06	117	0790840201^{X}	2016-12-06	23
NGC 5033	60601023002	2020-12-08	104	0871020101^{X}	2020-12-10	21
NGC 5283	60465006002	2018-11-17	33	00 088 264 001	2018-11-17	7
NGC 5290	60160554002	2021-07-28	19	00011388002–	2019-05-07	9
				00 011 388 007	to 2020-05-26	
NGC 5899	60061348002	2014-04-08	24	00 080 683 001	2014-04-08	7
NGC 6232	60061328002	2013-08-17	18	00080537001–02	2013-08-17 – 18	7
NGC 7213	60001031002	2014-10-05	102	00 080 811 001	2014-10-06	2
NGC 7674	60001151002	2014-09-30	52	0200660101^{X*}	2004-06-02	10
Mrk 18	60061088002	2013-12-15	20	00 080 406 001	2013-12-15	7
Mrk 273	60002028002	2013-11-04	70	0722610201^{X}	2013-11-04	23
ARP 102B	60160662002	2015-11-24	22	00 081 204 001	2015-11-24	7
ESO 253–003	60 101 014 002	2015-08-21	23	0762920501^{X}	2015-08-19	27
ESO 506–027	60469006002	2019-06-26	19	0312191801^{X*}	2006-01-24	12
HE 1136–2304	80 002 031 003	2014-07-02	64	0741260101^{X}	2014-07-02	110
IC 4518A	60 061 260 002	2013-08-02	8	00080141001	2013-08-02	7
IGC J11366–6002	60 061 213 002	2014-10-29	22	00080058001–02	2014-10-29 – 30	7
UGC 12 282	60160812002	2019-11-18	29	00 081 292 001	2019-11-18	7
LEDA 96 373	60061073002	2014-07-31	22	00 080 382 001	2014-07-31	4
LEDA 214543	60061273002	2017-02-06	21	00 080 172 001	2017-02-06	6
Z 367–9	60061270002	2014-12-21	30	00080158001–	2014-09-22	13
				00 080 158 002	2014-12-21	

Note. ^{X} marks the *XMM–Newton* observations. * indicates non-simultaneous observations of *NuSTAR* and *XMM–Newton*.

2.3.1 *XMM–Newton*

We used *XMM–Newton* (Jansen et al. 2001) EPIC/PN observations in the 0.5–10 keV energy range in our analysis. The data files were reduced using the Standard Analysis Software (SAS) version 20.0.0. The raw PN event files were processed using EPCHAIN task. We checked for particle background flare in the 10–12 keV energy range. The Good Time Interval file was generated using the SAS task TABGTIGEN. The source and background spectra were extracted from a circular region of 30 arcsec centred at the position of the optical counterpart and from a circular region of 30 arcsec radius away from the source, respectively. The background region is selected in the same CCD where no other X-ray sources are present. Using ESPECGET task, we generated the source and background spectra. We checked for pileup using the EPATPLOT task. We did not find any source that suffered from the pileup.

We used *XMM–Newton* spectra for 13 objects. For eight sources, the *XMM–Newton* observations were made simultaneously with the *NuSTAR*. For the rest five sources, we used non-simultaneous observations. For the non-simultaneous observations with *XMM–Newton*, and *NuSTAR*, we checked for spectral variability. The spectral variability is presented in detail in Section A. The detailed observation log is tabulated in Table 2.

3 ANALYSIS

3.1 Spectral analysis

The spectral analysis of combined spectra in the 0.5–150 keV range was performed in XSPEC v12.10 (Arnaud 1996). For our analysis, we adopted the cross-section from Verner et al. (1996), and ANGR abundances (Anders & Grevesse 1989). We used cross-normalization constants between the FPMA, FPMB, and BAT (Madsen et al. 2015, 2017) instruments while carrying out simultaneous spectral fitting.

We started X-ray spectral modelling using an absorbed power-law model with a cutoff at high energy. In XSPEC, the model reads as ZPHABS∗ZCUTOFF. We also added another component in the model for the absorption due to the Compton scattering, modelled with CABS. A component for the scattered primary emission, modelled with CONSTANT∗ZCUTOFF was added (e.g. Gupta et al. 2021). For the reprocessed emission, we used the convolution model REFLECT.[8] (Magdziarz & Zdziarski 1995). REFLECT is a generalization of the widely used PEXRAV model. It describes the reflection from a cold, neutral semi-infinite slab. The model parameters are reflection

[8]https://heasarc.gsfc.nasa.gov/xanadu/xspec/manual/node297.html

fraction (R), inclination angle (i), iron abundance (A_{Fe}), and metal abundances (A_M). We also added a Gaussian function at ∼6.4 keV to incorporate the iron K-line emission. For the soft-excess emission, we added a BLACKBODY model. However, one can also use the POWERLAW to approximate the soft-excess (e.g. Nandi et al. 2021). The model setup (hereafter Model-1a) reads in XSPEC as,

CONST1∗PHABS1∗(ZPHABS2∗CABS∗REFLECT∗ZCUTOFFPL1 + GAUSS + CONST2∗CUTOFFPL2 + BLACKBODY).

where, PHABS1 represents the Galactic absorption and is calculated using NH[9] tools of FTOOLs (HI4PI Collaboration 2016). CONST1 represents the cross-normalization factor between the FPMA, FPMB, and BAT. The ZPHABS2∗CABS∗ZCUTOFFPL1 represents the absorbed direct primary emission. CONST2∗CUTOFFPL represents the scattered primary emission, while CONST2 is the scattering fraction (f_{Scat}). The photon index (Γ), cutoff energy (E_{cut}), normalization of CUTOFFPL1 and ZCUTOFFPL2 are linked together. The column densities of the CABS and ZPHABS2 models are tied together and represent the line-of-sight obscuration towards the AGNs. We fixed the A_{Fe} and A_M at the Solar values, i.e. 1 and the inclination angle at 60° in our analysis. We allowed the Gaussian parameters to vary freely. However, when we could not constrain, we fixed the line energy at 6.4 keV and line width at 0.01, 0.05, or 0.1 keV, depending on the initial fitting.

We obtained good fit for all the sources using Model-1a. We noticed that the soft-excess is present in seven sources, namely, NGC 2655, NGC 4102, NGC 4258, NGC 5033, NGC 5290, NGC 7213, and HE 1136–2304. The spectra of the rest 23 sources can be fitted without the BLACKBODY component in Model-1a. The scattered emission is present in 15 sources in our sample. The photon index (Γ) and cutoff energy (E_{cut}) were obtained from the fitting. The hot electron temperature of the corona (kT_e) can be calculated from the cutoff energy, using the empirical relation $E_{cut} = 2kT_e$ (for $\tau_e < 1$) or $E_{cut} = 3kT_e$ (for $\tau_e > >1$) (Petrucci et al. 2001). Instead of this, one may also use Comptonization models such as COMPTT (Titarchuk 1994) or NTHCOMP (Zdziarski, Johnson & Magdziarz 1996; Zdziarski, Lubiński & Smith 1999) to obtain the hot electron temperature. To use the Comptonization model to probe the corona, we replaced CUTOFFPL with the NTHCOMP in the Model-1a. The spectral model reads in XSPEC as (hereafter Model-1b),

CONST1∗PHABS1∗(ZPHABS2∗CABS∗REFLECT∗NTHCOMP + GAUSSIAN + CONST2∗NTHCOMP + BLACKBODY).

During the spectral fitting, we froze the seed photon temperature of NTHCOMP component at 10 eV, which is a reasonable assumption for the SMBH with $M_{BH} > 10^7$ $M_\odot$ (e.g. Shakura & Sunyaev 1973; Makishima et al. 2000). We verified that the variations of the seed photon temperature from 5 to 20 eV did not affect the spectral fitting. We obtained good fits for all the sources with Model-1b. Table C1 shows the results obtained by applying Model-1a and Model-1b in our spectral fitting.

Next, we replaced REFLECT with a torus-based physically motivated model BORUS[10] (Baloković et al. 2018) in Model-1a. The `borus02` model consists of a spherical homogeneous torus with two polar cutouts in a conical shape. The torus covering factor and the inclination angle are the free parameters in the model. The `borus02` model also allows us to separate the line of sight column density (N_H^{los}) from the torus/obscuring material column density (N_H^{tor}). We did not require the Gaussian function while fitting with the `borus02` model, as `borus02` self-consistently calculates the Fe kα and Fe Kβ lines. In our fitting, we also fixed the torus covering factor at 0.5 and the inclination angle at 60°. The spectral model reads in XSPEC as (hereafter Model-2a),

CONST1∗PHABS1∗(ZPHABS2∗CABS∗ZCUTOFFPL1 + BORUS02 + CONST2∗CUTOFFPL2 + BLACKBODY).

The Model-2a gave us a good fit for all the sources in our sample. We obtained N_H^{los}, N_H^{tor}, Γ, and E_{cut} from the spectral modelling with Model-2a. As in the case of Model-1, to probe the corona with the Comptonized model, we replaced CUTOFFPL and `borus02`, with NTHCOMP and `borus12` models, respectively, in Model-2a. In the `borus12` model, the primary emission is described by NTHCOMP, replacing the CUTOFFPL model. The torus structure and geometry remain the same. This spectral model reads as (hereafter Model-2b),

CONST1∗PHABS1∗(ZPHABS2∗CABS∗NTHCOMP + BORUS12 + CONST2∗NTHCOMP + BLACKBODY).

During fitting with the `borus02` model, we linked Γ, E_{cut}, and normalization of CUTOFFPL1, CUTOFFPL2, and `borus02` together. The spectral analysis with the `borus12` model returned with a good fit for all the sources. Table C2 shows the results obtained from our spectral fitting by applying Model-2a and Model-2b. Figure 2 shows the representative spectrum of NGC 4507 in the top panel. In the middle and bottom panels, the χ distributions are shown while using Model-1 and Model-2, respectively.

To estimate the uncertainties in the parameters, we ran the STEPPAR command in XSPEC. The uncertainties are estimated at 68, 90 , and

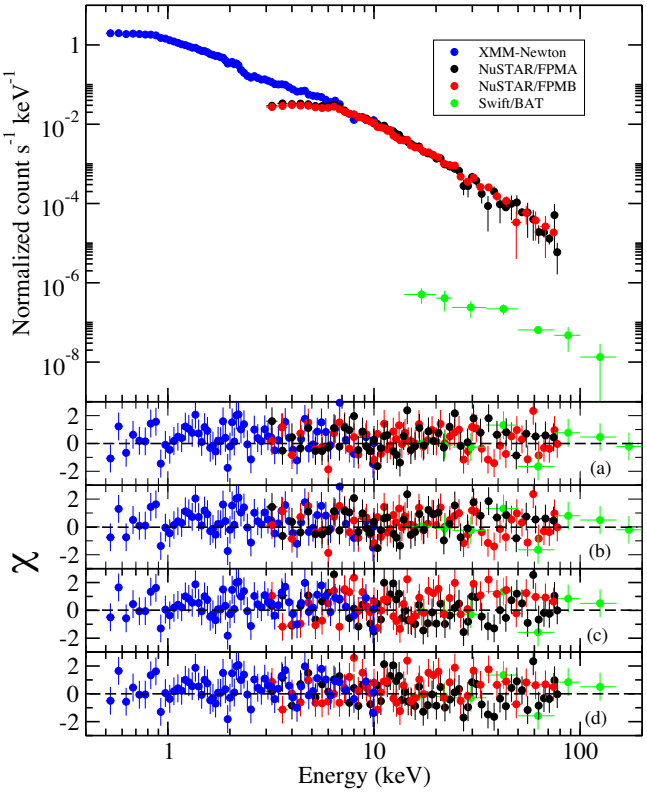

Figure 2. Top panel: Representative spectrum of NGC 4579. The black, red, and green circles represent the data from the FPMA, FPMB, and BAT instruments, respectively. The distributions of χ are shown in the middle and bottom panels, obtained from fitting the data with (a) Model-1a, (b) Model-1b, (c) Model-2a, and Model-2d, respectively.

[9] https://heasarc.gsfc.nasa.gov/cgi-bin/Tools/w3nh/w3nh.pl
[10] https://sites.astro.caltech.edu/~mislavb/download/

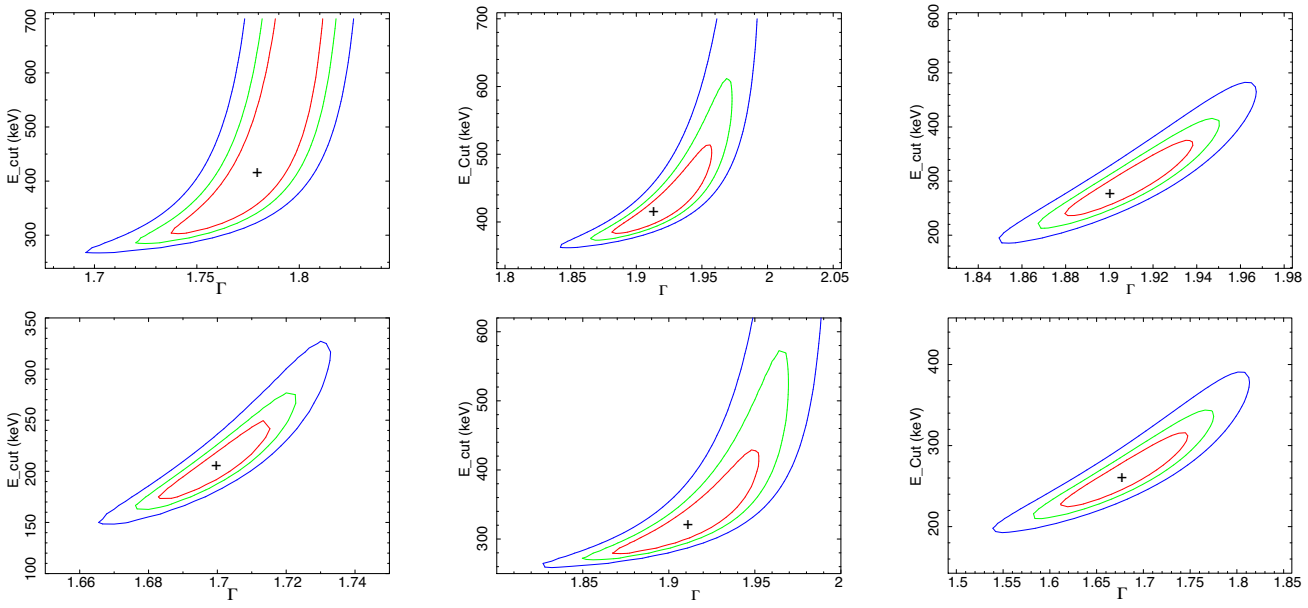

Figure 3. Confidence contours between the photon index (Γ) and cutoff energy ($E_{\rm cut}$) are shown for NGC 454E (top left), NGC 3147 (top middle), NGC 3998 (top right), NGC 4102 (bottom left), NGC 7213 (bottom middle), and HE 1136–2304 (bottom right). The red, green, and blue contours represent 1σ, 2σ, and 3σ levels, respectively.

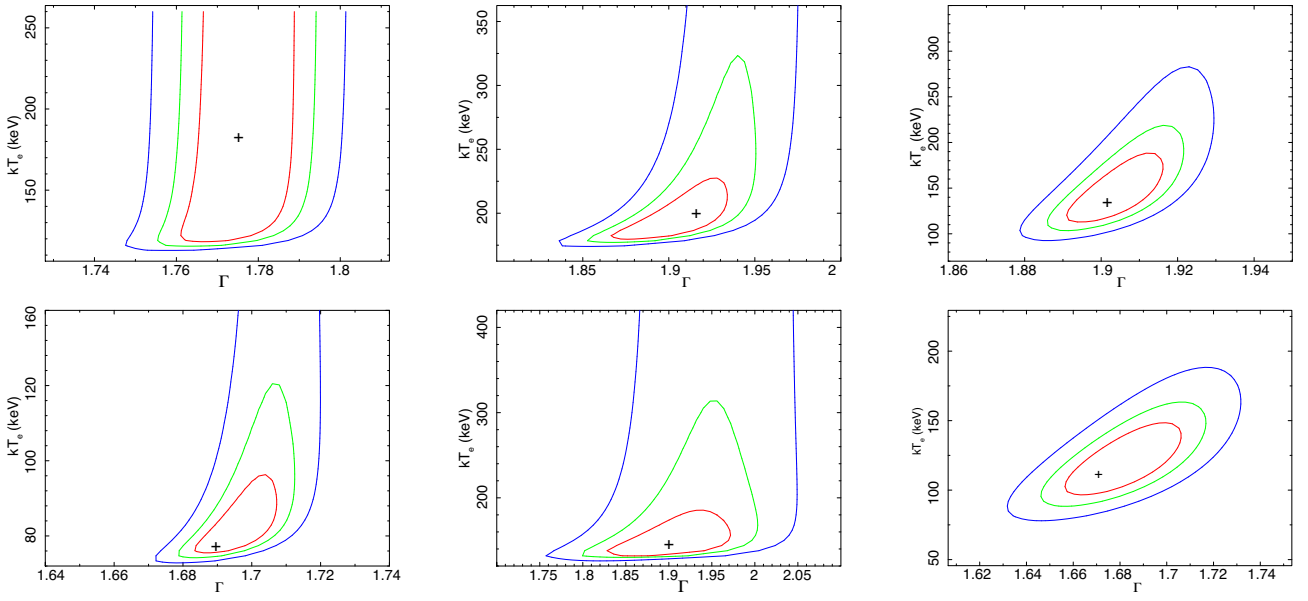

Figure 4. Confidence contours between the photon index (Γ) and hot electron temperature ($kT_{\rm e}$) are shown for NGC 454E (top left), NGC 3147 (top middle), NGC 3998 (top right), NGC 4102 (bottom left), NGC 7213 (bottom middle), and HE 1136–2304 (bottom right). The red, green, and blue contours represent 1σ, 2σ, and 3σ levels, respectively.

99 per cent confidence levels. We quoted uncertainties at 90 per cent confidence level throughout the paper unless mentioned otherwise. We show confidence contours between the Γ and the $E_{\rm cut}$ in Fig. 3 for NGC 454E, NGC 3147, NGC 3998, NGC 4102, NGC 7213, and HE 1136–2304 obtained from the fitting with Model-2a. Figure 4 shows the confidence contours between the Γ and the $kT_{\rm e}$, obtained from the spectral analysis of data with Model-2b for NGC 454E, NGC 3147, NGC 3998, NGC 4102, NGC 7213, and HE 1136–2304. In Fig. 3 (Fig. 4), we selected six sources randomly to show that $E_{\rm cut}$ ($kT_{\rm e}$) could not be constrained in all sources. Detailed spectral analysis result is tabulated in Table C2.

We also ran Markov Chain Monte Carlo (MCMC) in XSPEC[11] to calculate the uncertainty. Using the Goodman–Weare algorithm, the chains were run with eight walkers for a total of 10^6 steps. We discarded first 10 000 steps of the chains, assuming them to be in the 'burn-in' phase. Figure D1 shows the posterior distribution of the spectral parameters and errors obtained with the Model-2a and

[11] https://heasarc.gsfc.nasa.gov/xanadu/xspec/manual/node43.html

Model-2b in the left-hand and right-hand panels, respectively, for NGC 5033.

3.2 Estimation of parameters

The spectral analysis is carried out with four different models, with the differences in the choice of the primary continuum (CUTOFFPL or NTHCOMP), and reprocessed emission (REFLECT or BORUS). We obtained similar results with all four models. The common parameters in all four models are Γ and $N_{\rm H}^{\rm los}$. The mean value of Γ is obtained to be 1.73 ± 0.05, 1.73 ± 0.06, 1.74 ± 0.04, and 1.75 ± 0.04, from Model-1a, Model-1b, Model-2a, and Model-2b, respectively. The mean value of $N_{\rm H}^{\rm los}$is found to be log $N_{\rm H}^{\rm los}23.39 \pm 0.08$, 23.38 ± 0.10, 23.40 ± 0.09, and 23.40 ± 0.10 from the spectral fitting with the Model-1a, Model-1b, Model-2a, and Model-2b, respectively. The mean values of $E_{\rm cut}$ and $kT_{\rm e}$ are also similar within uncertainties from different models. As Model-1 and Model-2 returned similar values of the spectral parameters, we used the spectral results from Model-2 in the rest of the paper or mentioned otherwise.

For 24 sources, we used black hole mass from the BAT AGN Spectroscopic Survey (BASS; Koss et al. 2017; Ricci et al. 2017a; Koss et al. 2022). For the remaining six sources, we searched for the black hole mass in the literature (see Table 1). From the spectral fitting, we estimated the intrinsic luminosity ($L_{\rm int}$) of the sources in the 2–10 keV energy range. The bolometric luminosity is obtained by using the bolometric correction factor 10 (Vasudevan & Fabian 2009). We calculated the Eddington ratio as $\lambda_{\rm Edd} = L_{\rm bol}/L_{\rm Edd}$, where $L_{\rm Edd}$ is the Eddington luminosity and given by, $L_{\rm Edd} = 1.3 \times 10^{38}\ (M_{\rm BH}/{\rm M}_{\odot})$ erg s^{-1}.

The Γ, $kT_{\rm e}$, and $E_{\rm cut}$ were obtained from the spectral fitting. The optical depth of the corona is estimated by using the following relation (Zdziarski et al. 1996),

$$\tau_{\rm e} \approx -\frac{3}{2} + \sqrt{\frac{9}{4} + \frac{3}{\theta(\Gamma-1)(\Gamma+2)}}, \quad (1)$$

where $\theta = kT_{\rm e}/m_{\rm e}c^2$ is the dimensionless temperature.

The dimensionless compactness parameter is calculated using the following equation (e.g. Fabian et al. 2015, 2017):

$$l = 4\pi \frac{m_p}{m_e} \frac{R_g}{R_{\rm X}} \frac{L_{\rm X}}{L_{\rm Edd}}, \quad (2)$$

where $R_{\rm X}$ is coronal size and $L_{\rm X}$ is the coronal luminosity in the 0.1–200 keV energy range. The 0.1–200 keV luminosity is calculated from the extrapolation of the best-fitted model. In this work, we used $R_{\rm X} = 10\ R_{\rm g}$ (e.g. Fabian et al. 2015).

In the Compton cloud, the seed photons are up-scattered by the hot electrons and gain energy (e.g. Sunyaev & Titarchuk 1980, 1985). The mean of the energy gained by photons per scattering can be estimated by the Compton-y parameter, $y = 4\theta\ \max(\tau_{\rm e}, \tau_{\rm e}^2)$ (e.g. Rybicki & Lightman 1979). On the other hand, the total energy gain also depends on the number of scattering of the photons before escaping the medium. The average number of scattering ($N_{\rm S}$) is given by, $N_{\rm S} = y/\theta$.

A strong jet is expected in a low-accreting regime (Fender & Belloni 2004). In general, the radio luminosity ($L_{\rm R}$) is considered a good proxy of the jet luminosity ($L_{\rm jet}$; e.g. Fender & Belloni 2004). We collected jet luminosity ($L_{\rm jet}$ or $L_{\rm R}$ at 1.4 GHz) of sources from the NASA Extragalactic Database (NED) archive[12]

[12]https://ned.ipac.caltech.edu/

We estimated several spectral parameters of our sample. The detailed results are presented in Table C3.

3.3 Correlations among coronal parameters

Correlations among several coronal parameters have been extensively studied in the past (e.g. Kamraj et al. 2018; Ricci et al. 2017a). Here, we explored such co-dependencies among various spectral parameters. We employed Pearson, Spearman, and Kendall rank correlations to understand the relations among numerous parameters vis-á-vis the accretion mechanism around the LAC-AGNs. The results of our correlation study are tabulated in Table 3. Overall, all three correlation studies yield similar results. In total, we examined 30 correlations from our study. We considered the correlation is significant if the p-value is less than 0.01. For nine pairs of parameters, we found the corresponding p-value as <0.01. We found a strong anticorrelation between $kT_{\rm e}$ and $E_{\rm cut}$. The $N_{\rm S}$ is observed to be strongly correlated with $kT_{\rm e}$ and $E_{\rm cut}$. We found moderate anticorrelations and correlations for three pairs of parameters each.

4 RESULTS AND DISCUSSION

We studied a sample of AGNs with low Eddington ratio ($\lambda_{\rm Edd} < 10^{-3}$) to understand their coronal properties at low accretion regime. In our study, we used combined *XMM–Newton*, *Swift*, and *NuSTAR* spectra in the 0.5–150 keV energy range. From the spectral study, we obtained diverse spectral parameters and correlations among them.

4.1 Constraints on the coronal parameters

The corona is characterized by several parameters, namely the photon index (Γ), hot electron temperature ($kT_{\rm e}$), cutoff energy ($E_{\rm cut}$), and optical depth ($\tau_{\rm e}$). We obtained Γ, $kT_{\rm e}$, and $E_{\rm cut}$ from the spectral analysis, while $\tau_{\rm e}$ is obtained using equation (1). Figure 5 shows the distribution of $E_{\rm cut}$, $kT_{\rm e}$, and $\tau_{\rm e}$ in our sample.

We are able to constrain $E_{\rm cut}$ in 22 sources out of a total of 30 sources considered in our sample. The $E_{\rm cut}$ is distributed in a wide range of ∼50–500 keV in our sample. The broad parameter space of $E_{\rm cut}$ is consistent with the other recent studies (e.g. Ricci et al. 2018; Baloković et al. 2020; Hinkle & Mushotzky 2021). We found that the lower limit of $E_{\rm cut}$ is below 50 keV for two sources when $E_{\rm cut}$ is not constrained. The median value of $E_{\rm cut}$ for our sample is found to be 238 ± 93 keV with mean $<E_{\rm cut}> = 241 \pm 84$ keV, when $E_{\rm cut}$ is constrained. However, these values do not represent the whole sample, as the sources with the unconstrained $E_{\rm cut}$ are not considered.

To constrain the mean and median of the whole sample, we performed 1000 Monte Carlo simulations for each value of $E_{\rm cut}$. For each simulation, the values of $E_{\rm cut}$ are substituted with the values selected randomly from a Gaussian distribution with the standard deviation given by the uncertainty. The lower limits (L) are substituted with the values randomly selected from a uniform distribution in the interval of [L, $E_{\rm C,\,max}$], where $E_{\rm C,max} = 1000$ keV. For each run, we calculated the median of all values and used the mean of 1000 simulations (see Ricci et al. 2017a, 2018, for details). We find that the mean of $E_{\rm cut}$ is 284 ± 102 KeV, while the median is 267 ± 110 keV. Our results are consistent with the results of Ricci et al. (2017a, 2018) and the studies of the cosmic X-ray background, which suggest that the mean cutoff energy of AGNs should be $\lesssim$300 keV (e.g. Gilli, Comastri & Hasinger 2007; Ueda et al. 2014; Ananna et al. 2020).

Using MODEL-2, we additionally constrained $kT_{\rm e}$ for those 22 sources. We found a lower limit for the other eight sources.

Table 3. Correlation among different parameters.

		Pearson correlation		Spearman correlation		Kendall correlation	
Parameter-1	Parameter-2	ρ	p	R	p	τ	p
λ_{Edd}	Γ	–0.22	0.24	–0.16	0.40	–0.12	0.36
λ_{Edd}	E_{cut}	–0.02	0.90	0.01	0.99	–0.01	0.94
λ_{Edd}	kT_e	–0.07	0.71	–0.01	0.95	–0.02	0.89
λ_{Edd}	τ_e	0.18	0.33	–0.02	0.90	–0.03	0.84
λ_{Edd}	M_{BH}	–0.45	<0.01	–0.46	0.01	–0.32	0.02
kT_e	Γ	0.34	0.01	0.40	0.02	0.29	0.02
kT_e	E_{cut}	0.97	<0.01	0.95	<0.01	0.85	<0.01
Γ	E_{cut}	0.32	0.08	0.40	0.03	0.28	0.03
Γ	τ_e	–0.64	<0.01	–0.56	<0.01	–0.41	<0.01
M_{BH}	τ_e	–0.11	0.61	–0.04	0.83	0.01	0.93
M_{BH}	kT_e	0.04	0.84	0.03	0.87	0.03	0.86
M_{BH}	E_{cut}	–0.07	0.69	–0.02	0.92	–0.02	0.91
L_{bol}	M_{BH}	0.49	<0.01	0.51	<0.01	0.40	<0.01
L_{bol}	Γ	–0.21	0.26	–0.23	0.22	–0.017	0.18
L_{bol}	kT_e	–0.11	0.56	–0.07	0.70	–0.06	0.62
L_{bol}	E_{cut}	–0.10	0.59	–0.07	0.71	–0.06	0.68
L_{bol}	τ_e	0.09	0.64	0.13	0.49	0.09	0.49
L_{bol}	λ_{Edd}	0.46	<0.01	0.41	<0.01	0.29	0.01
λ_{Edd}	N_H	0.08	0.68	–0.12	0.52	–0.09	0.49
L_{bol}	N_H	0.06	0.76	0.02	0.90	0.01	0.99
N_S	Γ	–0.65	<0.01	–0.56	<0.01	–0.41	<0.01
N_S	kT_e	–0.85	<0.01	− 0.97	<0.01	–0.89	<0.01
N_S	E_{cut}	–0.84	<0.01	–0.91	<0.01	− 0.76	<0.01
N_S	λ	0.19	0.31	–0.02	0.90	–0.03	0.84
N_S	L_{bol}	0.11	0.57	0.13	0.49	0.09	0.50
N_S	M_{BH}	–0.08	0.66	–0.04	0.83	0.01	0.93
L_{bol}	L_{jet}	0.60	<0.01	0.61	<0.01	0.49	<0.01
EW	L_{bol}	–0.58	0.01	–0.52	0.02	–0.39	0.02
EW	λ_{Edd}	–0.25	0.29	–0.14	0.54	–0.11	0.55
EW	$L_{X,\,44}$	–0.45	0.06	–0.31	0.06	–0.44	0.05

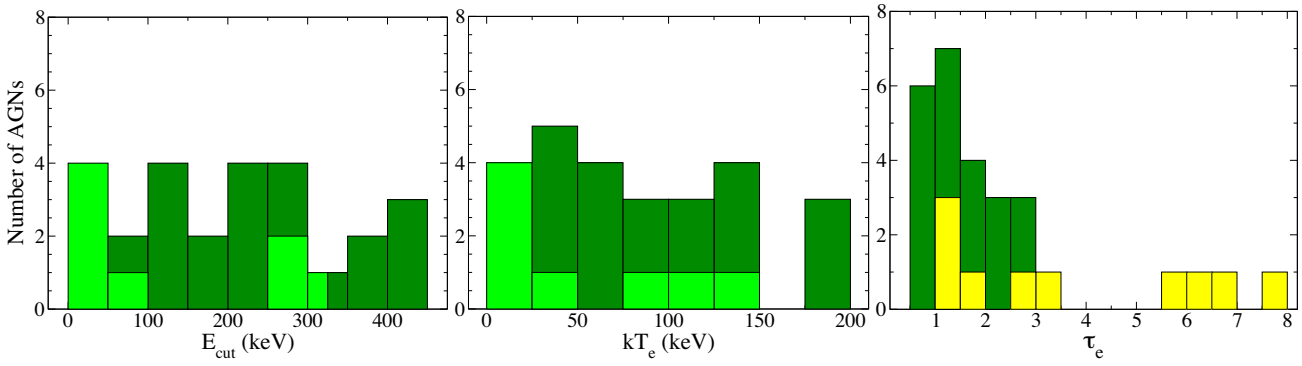

Figure 5. Histograms of cutoff energy (E_{cut}), hot electron plasma temperature (kT_e), and optical depth (τ_e) are shown in the left-hand, middle, and right-hand panels, respectively. The dark green bars represent the constrained parameters. The light green and yellow bars represent the lower limit and upper limit of the parameters, respectively.

Analogous to E_{cut}, kT_e was also obtained in a broad range between ∼10 and 300 keV which was found in other studies (e.g. Tortosa et al. 2018; Akylas & Georgantopoulos 2021). We obtained the lower limit of kT_e as 15 keV for IC 4518A, which is the lowest value among the sources in our samples. We calculated the mean and median of kT_e by running 1000 Monte Carlo simulations, as mentioned in the previous paragraph. We considered the maximum value of kT_e as 500 keV for the sources with the lower limit in the simulation. We found the mean value of our samples as $<kT_e> = 126 \pm 54$ keV with a median at 110 ± 45 keV.

As τ_e is calculated using kT_e, we also derived upper limits on τ_e for six observations. Excluding the upper limits, τ_e is observed to vary within the range of ∼0.5–3. The mean of the optical depth is estimated to be $<\tau_e> = 1.77 \pm 0.76$ with median $\tau_e = 1.47 \pm 0.58$ in our sample.

The corona remains hot for low-mass accretion rate AGNs as the cooling is inefficient. The hot corona also leads to high E_{cut} and optically thin medium ($\tau_e < 1$). Ricci et al. (2018) found the median of cutoff energy, $E_{cut} = 160 \pm 41$ keV for $\lambda_{Edd} > 0.1$, and $E_{cut} = 370 \pm 51$ keV for $L/L_{Edd} < 0.1$. As we explored an even lower Eddington ratio ($\lambda_{Edd} < 0.001$) regime, the median of the cutoff

energy is expected to be higher. However, this was not observed for our sample of low Eddington ratio AGN.

4.2 Dependence of the coronal properties on the Eddington ratio

In the current work, we studied a sample of AGNs with low $\lambda_{\rm Edd}$ to understand the coronal properties in the low accretion regime. The $\Gamma - \lambda_{\rm Edd}$ relation has been studied widely in the past (e.g. Gu & Cao 2009; Yang et al. 2015). A positive correlation is observed in HAC-AGN (e.g. Shemmer et al. 2006, 2008; Risaliti, Young & Elvis 2009; Brightman et al. 2013; Jana et al. 2020, 2021) while a negative correlation is found in the LLAGNs (e.g. Gu & Cao 2009; Younes et al. 2011; Hernández-García et al. 2013). The accretion mechanism differs in the low accretion state from the high accretion state. The opposite correlation indicates that the accretion mechanisms in different luminosity states are distinct.

The thin disc-corona model naturally explains the positive correlation in the high accretion state (e.g. Yang et al. 2015). In the high accreting regime ($\lambda_{\rm Edd} > 10^{-3}$), as the accretion rate increases, the number of seed photons increases, which cools the corona efficiently, producing the soft spectra. Contrary to that, the negative correlation in the low accretion state ($\lambda_{\rm Edd} < 10^{-3}$) could be explained with a hybrid truncated thin disc associated with hot accretion flow/corona and jet models (e.g. Gardner & Done 2013; Qiao & Liu 2013; Yang et al. 2015). In this scenario, due to the lack of matter supply, the inner disc evaporates into a hot accretion flow or corona (e.g. Esin et al. 1997; Yuan & Narayan 2014; Yang et al. 2015). As the mass accretion rate (or $\lambda_{\rm Edd}$) increases, the electron density and magnetic field strength increase, which in turn increases the synchrotron self-absorption depth. The self-absorbed synchrotron emission provides the seed photons for Comptonization. In this case, the hard X-ray flux ($L_{\rm X}$) increases more rapidly than the seed photon flux ($L_{\rm seed}$), which implies a negative correlation of $L_{\rm seed}/L_{\rm X}$ with $L_{\rm X}$. This leads to the negative correlation of the Γ and L_X or $\lambda_{\rm Edd}$ (e.g. Yang et al. 2015). If the accretion rate further reduces ($\lambda_{\rm Edd} < 10^{-6.5}$), the synchrotron emission from the jet dominates, leading to a saturation of the photon index at $\Gamma \sim 2$ (e.g. Plotkin, Gallo & Jonker 2013; Yang et al. 2015).

In our sample, $\lambda_{\rm Edd}$ spans the range $10^{-6.5} < \lambda_{\rm Edd} < 10^{-3}$, where a negative correlation of $\Gamma - \lambda_{\rm Edd}$ is expected. However, we did not find a significant correlation between Γ and $\lambda_{\rm Edd}$. The Pearson correlation coefficient between $\Gamma - \lambda_{\rm Edd}$ is -0.22 with p-value 0.24. Figure 6 shows the variation of Γ with the $\lambda_{\rm Edd}$. The solid red line represents the best linear fit. Using the linear regression method, we obtained $\Gamma = (-0.04 \pm 0.03)\log\lambda_{\rm Edd} + (1.59 \pm 0.13)$. The observed relation is weaker than the one found in previous studies. For examples, Gu & Cao (2009) found $\Gamma = (-0.09 \pm 0.03)\log\lambda_{\rm Edd} + (1.55 \pm 0.07)$, Younes et al. (2011) observed $\Gamma = (-0.31 \pm 0.06)\log\lambda_{\rm Edd} + (0.11 \pm 0.40)$, Jang et al. (2014) pointed $\Gamma = (-0.18 \pm 0.04)\log\lambda_{\rm Edd} + (0.66 \pm 0.25)$, and She et al. (2018) obtained $\Gamma = (-0.15 \pm 0.05)\log\lambda_{\rm Edd} + (1.0 \pm 0.03)$. Most of the previous studies were conducted using *Chandra* or *XMM–Newton* observations, which have a limited band-pass. Trakhtenbrot et al. (2017) found a shallower slope of the Γ–$\lambda_{\rm Edd}$ correlation with respect to previous studies, when considering the results obtained by broad-band X-ray spectroscopy. In the current work, we used high-quality broad-band spectra, though our sample is limited to 30 sources. Thus, we are unable to make a firm conclusion on the correlation/anticorrelation of $\lambda_{\rm Edd} - \Gamma$. Recently, Diaz et al. (2023) studied a sample of LLAGNs and found similar results. They argued that due to the small number of sources, they did not find a statistically significant correlation of Γ–$\lambda_{\rm Edd}$. We also inspected whether other spectral parameters are correlated with the $\lambda_{\rm Edd}$ and did not observe any correlation between $\lambda_{\rm Edd}$ and $kT_{\rm e}$, $\tau_{\rm e}$, or $E_{\rm cut}$.

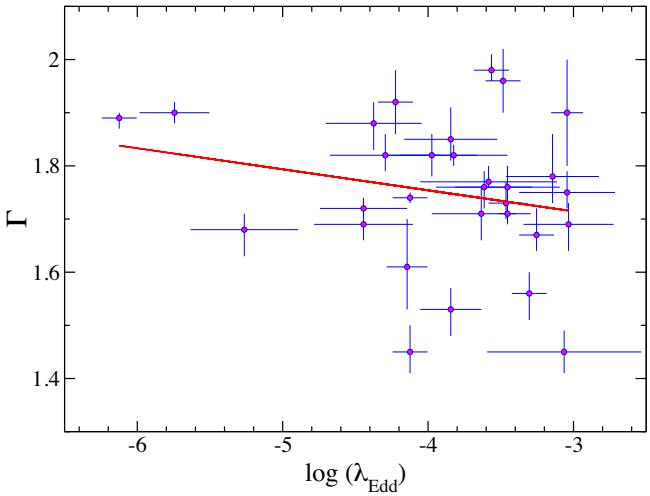

Figure 6. The photon index (Γ) is plotted as a function of the Eddington ratio ($\lambda_{\rm Edd}$). The linear regression analysis gives $\Gamma = (-0.04 \pm 0.03)\log\lambda_{\rm Edd} + (1.59 \pm 0.13)$. The red line represents the best fit of the linear regression analysis.

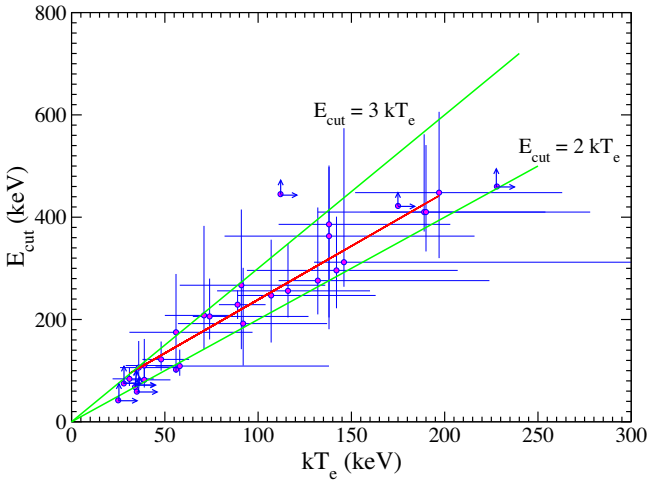

Figure 7. Relation between the hot electron temperature ($kT_{\rm e}$) and cutoff energy ($E_{\rm cut}$) is shown. The solid red line represents the best fit to the data. The best fit is $E_{\rm cut} = (2.10 \pm 0.12)kT_{\rm e} + (29.4 \pm 12.1)$. Two green solid lines represent the relation $E_{\rm cut} = 2kT_{\rm e}$ and $E_{\rm cut} = 3kT_{\rm e}$.

4.3 Dependency of the coronal properties on the $kT_{\rm e}$

We found that $kT_{\rm e}$ and $E_{\rm cut}$ are strongly correlated (see Table 3) in our sample. The linear fitting yields $E_{\rm cut} = (2.10 \pm 0.12)kT_{\rm e} + (29.4 \pm 12.1)$. Figure 7 shows that all the 22 sources with constrained $E_{\rm cut}$ and $kT_{\rm e}$ lie within the $E_{\rm cut} = 2kT_{\rm e}$ and $E_{\rm cut} = 3kT_{\rm e}$ lines. This agrees with the empirical approximation of $E_{\rm cut} \approx 2 - 3\ kT_{\rm e}$ (Petrucci et al. 2001). However, Middei et al. (2019) argued that the empirical relation only holds for low $\tau_{\rm e}$ and low $kT_{\rm e}$. They suggested that if the origin of X-rays is other than the thermal Comptonization, for example, synchrotron self Comptonization, the relation $E_{\rm cut} \sim 2$–$3\ kT_{\rm e}$ may not hold. The deviation from this relation has been observed in a few sources (e.g. Pal et al. 2022). We tested this relation from the spectral modelling with the REFLECT model

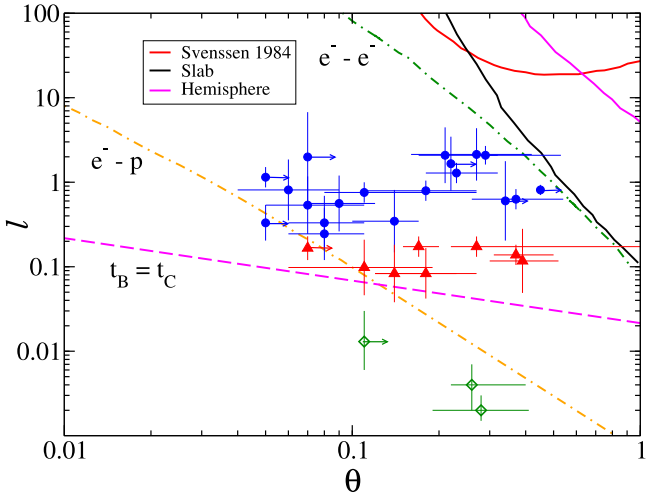

Figure 8. Compactness–temperature ($l - \theta$) diagram for our sample. Solid black and red lines correspond to pair production lines for slab and hemispherical geometries from Stern et al. (1995), respectively. The solid magenta line represents the pair production line from Svensson (1984). The orange dashed–dotted, green dashed–dotted, and magenta dashed lines represent the region where electron–electron coupling, electron–proton coupling, and bremsstrahlung cooling dominate, respectively. The blue circles, red triangles, and green diamonds represent the AGNs with $-3 > \log \lambda_{\rm Edd} > -4$, $-4 > \log \lambda_{\rm Edd} > -5$, and $\log \lambda_{\rm Edd} < -5$, respectively. The arrows represent the lower limit.

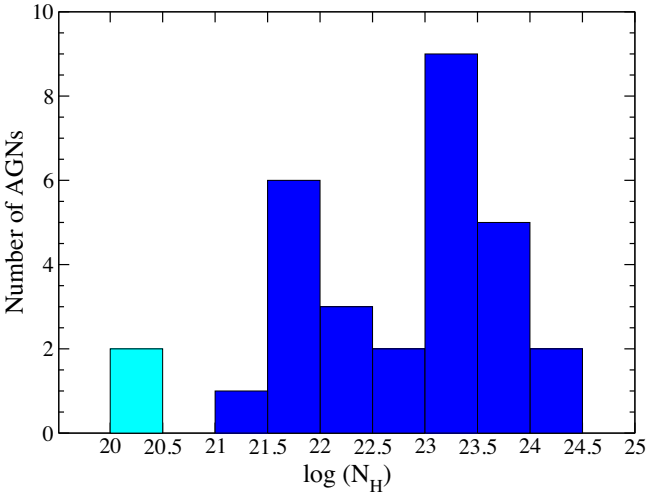

Figure 9. Histogram of the line of sight column density of our sample. The blue and cyan colours represent the constrained value and upper limit of $N_{\rm H}$, respectively.

(Model-1a and Model-1b). We obtained $E_{\rm cut} = (2.18 \pm 0.16)kT_{\rm e} + (25. \pm 17.2)$, which is similar to the findings with the BORUS model (Model-2a and Model-2b). None the less, our study found $E_{\rm cut} \approx 2\ kT_{\rm e}$ is an acceptable approximation for the LAC-AGNs.

We obtained a weak positive correlation between $kT_{\rm e}$ and Γ, with the Pearson correlation coefficient of 0.34 with a p-value of 0.01. For purely thermal Comptonization, a negative correlation between $kT_{\rm e}$ and Γ is expected. However, if there are non-thermal seed photons, e.g. synchrotron emission from a jet, a negative correlation may not hold (e.g. Yang et al. 2015). None the less, the observed relation indicates a complex process for the X-ray emission other than thermal Comptonization.

We calculated the average number of scatterings the photons suffered before escaping the Compton cloud (see Section 3.2). We find that $N_{\rm s}$ is anticorrelated with Γ having a Pearson correlation coefficient of -0.65 with $p < 0.01$, as presented in the earlier works (e.g. Sunyaev & Titarchuk 1980; Pozdnyakov et al. 1983). $N_{\rm S}$ is also found to be strongly anticorrelated with $kT_{\rm e}$ and $E_{\rm cut}$. The Pearson correlation index is obtained to be -0.85 with the p-value of <0.01 for $kT_{\rm e}$, and -0.85 with the p-value of <0.01 for $E_{\rm cut}$, respectively. This is expected as a high $kT_{\rm e}$ would lead the corona to be optically thin; hence, the lower value of $N_{\rm S}$. The anti-correlation between $N_{\rm S}$ and $kT_{\rm e}$ is also consistent with the previous simulations (e.g. Chatterjee, Chakrabarti & Ghosh 2017a, b). Compton scattering could induce X-ray polarization. The variation in the polarization caused by repeated scatterings could be detected above the minimum detectable polarization with the ongoing *Imaging X-ray Polarimetry Explorer* (Weisskopf et al. 2016) or future X-ray polarimetry missions, such as *XPoSat*.

4.4 The *l–θ* plane

We constructed the compactness–temperature ($l - \theta$) diagram in Fig. 8. Solid black and red lines correspond to the pair production lines for slab and hemispherical geometries from Stern et al. (1995). The solid magenta line represents the pair production line from Svensson (1984). The compactness (l) is calculated using equation (2).

The pair production is thought to be a fundamental process in AGN coronae due to photon–photon collisions (e.g. Svensson 1982a, b; Guilbert, Fabian & Rees 1983). This process could, in fact, lead to a runway pair production, which might act as a thermostat for the corona (e.g. Bisnovatyi-Kogan, Zel'dovich & Syunyaev 1971; Svensson 1984; Zdziarski 1985; Fabian et al. 2015, 2017). If that were the case, then the AGN would be expected to lie below the pair line. We found that all the sources are located below the theoretical pair lines for slab and hemispherical geometry. The sources in our sample are located around the electron–electron (e^-–e^-) and electron–proton (e^-–p) coupling lines, which could indicate the processes responsible for the cooling. We also found that three sources lie below the bremsstrahlung cooling line ($t_{\rm B} = t_{\rm C}$). All three sources, namely NGC 3718, NGC 3998, and UGC 12282, have $\lambda_{\rm Edd} < 10^{-5}$ and, as the Eddington ratio is directly proportional to the compactness, which leads to the low compactness (Ricci et al. 2018).

4.5 Obscuration properties

The covering factor of the circumnuclear obscuring materials has been found to decrease with increasing accretion rates (e.g. Ueda et al. 2003; Treister, Krolik & Dullemond 2008). However, recent work has shown that the obscuring material in nearby AGN is regulated by the Eddington ratio (Ricci et al. 2017b). It has been found that the covering factor is ~ 85 per cent for $\lambda_{\rm Edd} \sim 10^{-4}$–$10^{-1.5}$, and sharply decreases at $\lambda_{\rm Edd} > 10^{-1.5}$ (Ricci et al. 2017b). The obscuring material is expected to disappear at very low accretion rates (e.g. Elitzur 2008) due to the lack of outflowing material (e.g. Elitzur 2008). Ricci et al. (2022) suggested that an inactive AGN ($\lambda_{\rm Edd} < <10^{-4}$) starts accreting following an inflow of gas and dust (see also Ricci et al. 2017b). This increases both $N_{\rm H}$ and $\lambda_{\rm Edd}$. When $\lambda_{\rm Edd}$ reaches a critical value ($\lambda_{\rm Edd} \sim 10^{-1.5}$), the radiation pressure blows away the obscuring material. The AGN spends some time as unobscured ($N_{\rm H} < 10^{22}$ cm^{-2}) before moving back to the low $\lambda_{\rm Edd}$ state with low $N_{\rm H}$.

Figure 9 shows the histogram of our sample's line of sight column density. In our sample, we found that nine sources are unobscured ($N_{\rm H}^{\rm los} < 10^{22}$ cm^{-2}) and 21 sources are obscured ($N_{\rm H}^{\rm los} > 10^{22}$ cm^{-2}). Among the 21 obscured sources, two sources are Compton-thick

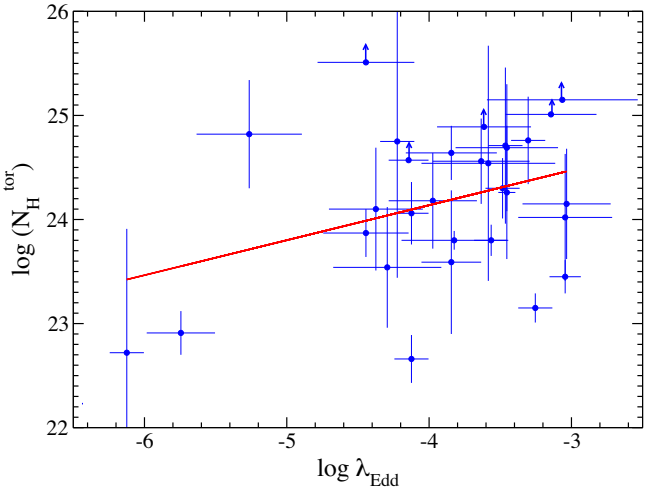

Figure 10. The variation of average density of the obscuring material (N_H^{tor}) as a function of the Eddington ratio (λ_{Edd}). The red line represents the linear best fit.

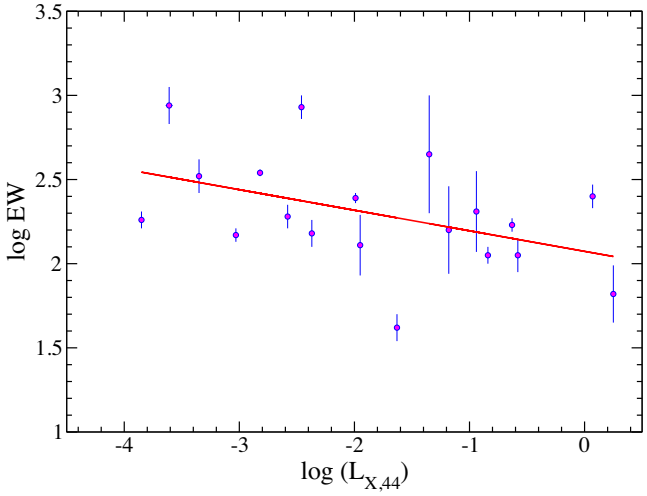

Figure 11. X-ray Baldwin effect. The EW of iron Kα line is plotted as a function of 2–10 keV X-ray luminosity ($L_{X,44}$). The EW and $L_{X,44}$ are in the unit of eV, and 10^{44} erg s^{-1}, respectively. The red line represents the linear best fit, with $\log \mathrm{EW} = (-0.12 \pm 0.09)\log L_{X,44} + (2.1 \pm 0.1)$.

($N_H^{los} > 10^{24}$ cm^{-2}) and 19 sources are Compton-thin ($N_H^{los} = 10^{22-24}$ cm^{-2}). We found two unobscured sources and one obscured source (one of them in CT) in an extremely low accretion region ($\lambda_{Edd} < 10^{-5}$). On the other hand, at $10^{-5} < \lambda_{Edd} < 10^{-3}$, we observed that seven sources are unobscured, and 20 sources are obscured. If we move towards the low accretion region ($\lambda_{Edd} < -5$), the fraction of obscured sources drops from $\sim 73^{+8}_{-9}$ per cent to $\sim 39^{+23}_{-20}$per cent.[13] The increasing fraction of unobscured sources towards the low-accretion regime supports the Eddington ratio regulated unification model (e.g. Ricci et al. 2017b, 2022).

We obtained the average density of the obscuring material (N_H^{tor}), which is responsible for the reprocessing emission. The median of N_H^{tor} is found to be $\log N_H^{tor} = 24.22 \pm 0.45$, which is higher than the N_H^{los}. The median of the line of sight column density is $\log N_H^{los} = 23.02 \pm 0.08$. We plot the variation of N_H^{tor} as a function of λ_{Edd} in Fig. 10. The linear regression analysis found that $\log N_H^{tor} = (0.34 \pm 0.04) \log \lambda_{Edd} + (25.5 \pm 0.5)$, suggesting a positive relation between λ_{Edd} and N_H^{tor}. This suggests that at low Eddington ratio, the average column density decreases. Diaz et al. (2023) also found a similar relation between N_H^{tor} and λ_{Edd}. The relation between N_H^{tor} and λ_{Edd} also supports the Eddington ratio regulated unification and growth model (e.g. Ricci et al. 2022).

4.6 Reprocessed emission

We obtained the reflection parameter (R) from Model-1a and Model-1b. From our analysis, it is found that R could be constrained only in 7 sources out of a total of 30 sources. As in case of E_{cut} and kT_e, we calculated the mean of R by running 1000 Monte Carlo simulations, with the range of R between 0 and 10. We found the mean $<R> = 0.25 \pm 0.08$ with a median of 0.26 ± 0.09. Ricci et al. (2017a) found a higher value of median of R as 0.53 ± 0.09 with a sample of 838 BAT AGNs. Our finding is consistent with the fact that the low-accreting AGNs show weak reflection (e.g. Ptak et al. 2004; Younes et al. 2011).

We modelled the Fe K-emission line with a Gaussian function while fitting the data with Model-1. Out of total of 30 sources, a Gaussian line is required in 28 objects. We did not find the iron Kα line for two sources: NGC 3147 and NGC 3998. We could constrain the equivalent width (EW) for 19 sources. We tested the so-called 'X-ray Baldwin effect', i.e. the correlation of EW with the X-ray luminosity in our sample (Iwasawa & Taniguchi 1993). Figure 11 shows the EW of Fe Kα line as a function of X-ray luminosity ($L_{X,44}$). The linear regression analysis returned as $\log \mathrm{EW} = (-0.12 \pm 0.09)\log L_{X,44} + (2.1 \pm 0.1)$, where EW and $L_{X,44}$ are in the unit of eV, and 10^{44} erg s^{-1}, respectively. This relation is consistent with the previous studies of the X-ray Baldwin effect (e.g. Bianchi et al. 2007; Ricci et al. 2013). We also checked the relation of EW with λ_{Edd}. The linear best-fitting result returned with $\log \mathrm{EW} = (-0.15 \pm 0.10)\log \lambda_{Edd} + (1.74 \pm 0.52)$. Our result is consistent with the previous studies (e.g. Ricci et al. 2013). The observed relation suggests that the reprocessing mechanism of LAC-AGNs is similar to the HAC–AGNs.

We did not find any correlation or anticorrelation of EW with the L_{2-10} keV, $L_{X,44}$, and λ_{Edd}. The small sample size could be the reason for not observing any correlation/anticorrelation of EW with other parameters.

4.7 Jet

In LAC-AGNs X-ray radiation is believed to be produced in a radiatively inefficient flow (e.g. Narayan & Yi 1994; Quataert 2001; Nemmen et al. 2014), or from the base of the jet (e.g. Markoff, Falcke & Fender 2001; Falcke, Körding & Markoff 2004). The observed jet luminosity (L_{jet})[14] is tabulated in Table 3. Figure 12 shows the histogram plots for the L_{bol} and the L_{jet} of our sample. The red dashed, and solid blue lines represent the L_{jet} and L_{bol}, respectively. We observed that the L_{jet} is higher than the L_{bol}[15] for every source in our sample. The L_{jet} is found to be ~0–3 orders of magnitude higher than the L_{bol}. If we consider ~ 5 per cent power of the jet is radiated away (e.g. Blandford & Königl 1979; Fender 2001), the total jet power (Q_{jet}) would be ~0–4 orders of

[13]The fractions are computed following Cameron (2011), and the reported uncertainties represent the 16th and 84th quantiles of a binomial distribution.

[14]L_{jet} is calculated from the L_R.

[15]The L_{bol} is calculated from the 2–10 keV X-ray luminosity (see Section 3)

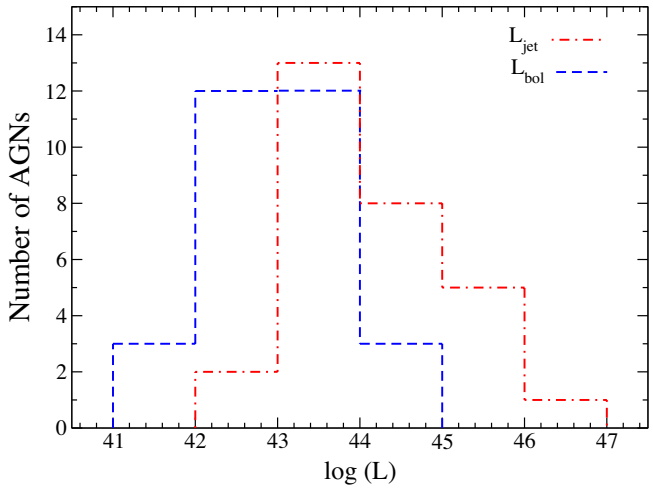

Figure 12. Histogram of the observed jet luminosity ($L_{\rm jet}$) and bolometric luminosity ($L_{\rm bol}$). The red dashed and solid blue lines represent the $L_{\rm jet}$ and $L_{\rm bol}$, respectively.

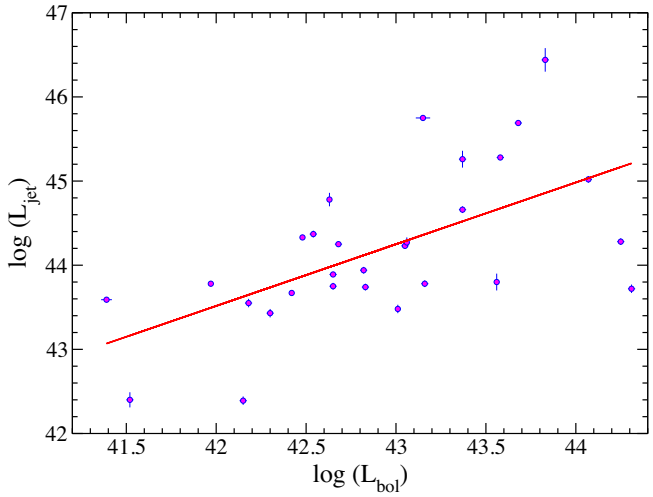

Figure 13. Variation of the jet luminosity $L_{\rm jet}$ as a function of Eddington ratio ($\lambda_{\rm Edd}$). The solid red line represents the best fit with linear regression. The slope of the fit is 0.68 ± 0.12.

magnitude higher than the bolometric luminosity ($L_{\rm bol}$). This is not uncommon for LLAGNs: Nagar, Falcke & Wilson (2005) studied a sample of LLAGNs and found $Q_{\rm jet}$ (also $L_{\rm jet}$) exceeds the $L_{\rm bol}$ by 0–4.5 magnitude with a mean around three orders in their sample. This study suggests that the jet luminosity greatly surpasses the accretion power in the LAC-AGNs.

Figure 13 shows the variation of the jet luminosity ($L_{\rm jet}$) with the bolometric luminosity ($L_{\rm bol}$). The solid red line represents the best linear fit $\log(L_{\rm jet}) = (0.68 \pm 0.12)\log(L_{\rm bol}) + (12.7 \pm 8.1)$ from the linear regression analysis. This relation is consistent with the standard radio–X-ray correlation of coefficient of ∼0.6–0.7 (e.g. Corbel et al. 2000, 2003; Gallo, Fender & Pooley 2003; Merloni et al. 2003; Körding, Fender & Migliari 2006; Gallo et al. 2014). The standard correlation is the relation between the radio and X-ray flux in the low hard state of black holes. Thus, the similar relation of $L_{\rm jet}$–$L_{\rm bol}$ for the present sample indicates a radiatively inefficient accretion flow in the LAC-AGNs.

5 CONCLUSION AND SUMMARY

We studied 30 low-accreting AGNs ($\lambda_{\rm Edd} < 10^{-3}$) using combined *Swift*, *XMM–Newton*, and *NuSTAR* data in 0.5–150 keV range. For the spectral analysis, we used the convolution model REFLECT and torus-based physically motivated BORUS model combined with either the CUTOFFPL or the NTHCOMP model for the continuum. Several parameters, namely the photon index, cutoff energy, and hot electron temperature of the corona, are estimated directly from the spectral fitting. Other parameters, such as the optical depth, the number of scatterings, and compactness, are calculated using spectral parameters. We inspected correlations among several parameters to understand the accretion dynamics in the low accreting region.

We summarize our work as follows.

(i) We studied 30 low-accreting AGNs ($\lambda_{\rm Edd} < 10^{-3}$) using combined *Swift*, *XMM–Newton*, and *NuSTAR* data to understand the accretion properties at low accretion region.

(ii) We did not find any significant correlation between the photon index (Γ) and Eddington ratio ($\lambda_{\rm Edd}$), contrary to the previous studies in the low-accretion domain.

(iii) We found that the hot electron temperature ($kT_{\rm e}$) is related to the cutoff energy ($E_{\rm cut}$) as $E_{\rm cut} = (2.10 \pm 0.12)kT_{\rm e} + (29.4 \pm 12.1)$.

(iv) We noticed that all the sources are located well below the pair production line in the compactness–temperature ($l - \theta$) diagram. We note that the cooling process is complex in the low accretion region.

(v) We observed the so-called 'X-ray Baldwin effect' in low-accretion regime. The EW of the Fe Kα line is found to be related with the X-ray luminosity ($L_{\rm X,44}$) and Eddington ratio ($\lambda_{\rm Edd}$) as $\log {\rm EW} = (-0.12 \pm 0.09)\log L_{\rm X,44} + (2.1 \pm 0.1)$ and $\log {\rm EW} = (-0.15 \pm 0.10)\log \lambda_{\rm Edd} + (1.74 \pm 0.52)$.

(vi) The jet luminosity ($L_{\rm jet}$) is related with the bolometric luminosity as $L_{\rm jet} \propto L_{\rm bol}^{0.7}$. This relation is consistent with the standard radio-X-ray correlation for Galactic black hole X-ray binary in the low hard state. This supports the presence of a radiatively inefficient accretion flow in the LAC-AGNs.

(vii) We observed that the fraction of the unobscured sources increases as the Eddington ratio decreases. This support the Eddington ratio regulated unification model of AGNs.

In this work, we studied the coronal properties of AGNs with the Eddington ratio ranges in $\lambda_{\rm Edd} \sim 10^{-6.5}$–$10^{-3}$. In the future, we will add more AGNs to our sample with an even lower Eddington ratio. Future broad-band hard X-ray missions, such as *HEX-P* (Madsen et al. 2018), could allow us to constrain $E_{\rm cut}$ with better accuracy and expand our understanding of such systems profoundly. On the other hand, the large effective area and high throughput of *Colibrì* (Caiazzo et al. 2019; Heyl et al. 2019) would be able to extend the population of LLAGNs as well as provide crucial information related to the line of sight $N_{\rm H}$ distribution (Ricci et al. 2017b) of them.

ACKNOWLEDGEMENTS

We thank the anonymous reviewers for their constructive suggestions which helped to improve the paper. AJ and HK acknowledge the support of the grant from the Ministry of Science and Technology of Taiwan with the grand number MOST 110-2811-M-007-500 and MOST 111-2811-M-007-002. HK acknowledge the support of the grant from the Ministry of Science and Technology of Taiwan with the grand number MOST 110-2112-M-007-020 and MOST-111-2112-M-007-019. AC and SSH are supported by the Canadian Space Agency and the Natural Sciences and Engineering Research Council of Canada. CR acknowledges support from the Fondecyt Iniciacion

grant 11190831 and ANID BASAL project FB210003. Research at Physical Research Laboratory is supported by the Department of Space, Government of India, for this work. This research has made use of data and/or software provided by the High Energy Astrophysics Science Archive Research Center (HEASARC), which is a service of the Astrophysics Science Division at NASA/GSFC and the High Energy Astrophysics Division of the Smithsonian Astrophysical Observatory. This work has made use of data obtained from the *NuSTAR* mission, a project led by Caltech, funded by NASA and managed by NASA/JPL, and has utilized the NuSTARDAS software package, jointly developed by the ASDC, Italy and Caltech, USA. This research has made use of observations obtained with *XMM–Newton*, an ESA science mission with instruments and contributions directly funded by ESA Member States and NASA. This work made use of XRT data supplied by the UK Swift Science Data Centre at the University of Leicester, UK.

DATA AVAILABILITY

We used archival data of *NuSTAR, Swift and XMM-Newton* observatories for this work. All the models used in this work are publicly available. Appropriate links are given in the text.

REFERENCES

Akylas A., Georgantopoulos I., 2021, A&A, 655, A60
Ananna T. T., Treister E., Urry C. M., Ricci C., Hickox R. C., Padmanabhan N., Marchesi S., Kirkpatrick A., 2020, ApJ, 889, 17
Anders E., Grevesse N., 1989, Geochim. Cosmochim. Acta, 53, 197
Arnaud K. A., 1996, in Jacoby G. H., Barnes J., eds, ASP Conf. Ser. Vol. 101, Astronomical Data Analysis Software and Systems V. Astron. Soc. Pac., San Francisco, p. 17
Arnaud K. A. et al., 1985, MNRAS, 217, 105
Baloković M. et al., 2018, ApJ, 854, 42
Baloković M. et al., 2020, ApJ, 905, 41
Bianchi S., Guainazzi M., Matt G., Fonseca Bonilla N., 2007, A&A, 467, L19
Bisnovatyi-Kogan G. S., Zel'dovich Y. B., Syunyaev R. A., 1971, Sov. Astron., 15, 17
Blandford R. D., Königl A., 1979, ApJ, 232, 34
Brightman M. et al., 2013, MNRAS, 433, 2485
Brightman M. et al., 2018, ApJ, 867, 110
Caiazzo I. et al., 2019, Unveiling the secrets of black holes and neutron stars with high-throughput, high-energy resolution X-ray spectroscopy. Zenodo. Available at: https://doi.org/10.5281/zenodo.3824441
Cameron E., 2011, PASA, 28, 128
Chakrabarti S., Titarchuk L. G., 1995, ApJ, 455, 623
Chartas G., Kochanek C. S., Dai X., Poindexter S., Garmire G., 2009, ApJ, 693, 174
Chatterjee A., Chakrabarti S. K., Ghosh H., 2017a, MNRAS, 465, 3902
Chatterjee A., Chakrabarti S. K., Ghosh H., 2017b, MNRAS, 472, 1842
Corbel S., Fender R. P., Tzioumis A. K., Nowak M., McIntyre V., Durouchoux P., Sood R., 2000, A&A, 359, 251
Corbel S., Nowak M. A., Fender R. P., Tzioumis A. K., Markoff S., 2003, A&A, 400, 1007
Dadina M., 2007, A&A, 461, 1209
de Rosa A. et al., 2012, MNRAS, 420, 2087
Diaz Y. et al., 2023, A&A, 669, A114
Done C., Gierliński M., Kubota A., 2007, A&AR, 15, 1
Done C., Davis S. W., Jin C., Blaes O., Ward M., 2012, MNRAS, 420, 1848
Elitzur M., 2008, New Astron. Rev., 52, 274
Esin A. A., McClintock J. E., Narayan R., 1997, ApJ, 489, 865
Evans P. A. et al., 2009, MNRAS, 397, 1177
Fabian A. C. et al., 2009, Nature, 459, 540
Fabian A. C., Lohfink A., Kara E., Parker M. L., Vasudevan R., Reynolds C. S., 2015, MNRAS, 451, 4375
Fabian A. C., Lohfink A., Belmont R., Malzac J., Coppi P., 2017, MNRAS, 467, 2566
Falcke H., Körding E., Markoff S., 2004, A&A, 414, 895
Fender R. P., 2001, MNRAS, 322, 31
Fender R., Belloni T., 2004, ARA&A, 42, 317
Foreman-Mackey D., 2016, J. Open Source Softw., 1, 24
Gallo E., Fender R. P., Pooley G. G., 2003, MNRAS, 344, 60
Gallo E. et al., 2014, MNRAS, 445, 290
Gardner E., Done C., 2013, MNRAS, 434, 3454
George I. M., Fabian A. C., 1991, MNRAS, 249, 352
Gilli R., Comastri A., Hasinger G., 2007, A&A, 463, 79
Gu M., Cao X., 2009, MNRAS, 399, 349
Guilbert P. W., Fabian A. C., Rees M. J., 1983, MNRAS, 205, 593
Gupta K. K. et al., 2021, MNRAS, 504, 428
HI4PI Collaboration, 2016, A&A, 594, A116
Haardt F., Maraschi L., 1991, ApJ, 380, L51
Harrison F. A. et al., 2013, ApJ, 770, 103
Hernández-García L., González-Martín O., Márquez I., Masegosa J., 2013, A&A, 556, A47
Heyl J. et al., 2019, Bull. Am. Astron. Soc., 51, 175
Hinkle J. T., Mushotzky R., 2021, MNRAS, 506, 4960
Ho L. C., 2009, ApJ, 699, 626
Iwasawa K., Taniguchi Y., 1993, ApJ, 413, L15
Jana A., Chatterjee A., Kumari N., Nandi P., Naik S., Patra D., 2020, MNRAS, 499, 5396
Jana A., Kumari N., Nandi P., Naik S., Chatterjeee A., Jaisawal G. K., Hayasaki K., Ricci C., 2021, MNRAS, 507, 687
Jang I., Gliozzi M., Hughes C., Titarchuk L., 2014, MNRAS, 443, 72
Jansen F. et al., 2001, A&A, 365, L1
Kamraj N., Harrison F. A., Baloković M., Lohfink A., Brightman M., 2018, ApJ, 866, 124
Kamraj N. et al., 2022, ApJ, 927, 42
Kara E., Fabian A. C., Cackett E. M., Uttley P., Wilkins D. R., Zoghbi A., 2013, MNRAS, 434, 1129
Kawamuro T., Ueda Y., Tazaki F., Terashima Y., Mushotzky R., 2016, ApJ, 831, 37
Körding E. G., Fender R. P., Migliari S., 2006, MNRAS, 369, 1451
Koss M. et al., 2017, ApJ, 850, 74
Koss M. J. et al., 2022, ApJS, 261, 2
Lohfink A. M., Reynolds C. S., Miller J. M., Brenneman L. W., Mushotzky R. F., Nowak M. A., Fabian A. C., 2012, ApJ, 758, 67
Madsen K. K. et al., 2015, ApJS, 220, 8
Madsen K. K., Forster K., Grefenstette B. W., Harrison F. A., Stern D., 2017, ApJ, 841, 56
Madsen K. K. et al., 2018, in den Herder J.-W. A., Nikzad S., Nakazawa K., eds, Proc. SPIE Conf. Ser. Vol. 10699, Space Telescopes and Instrumentation 2018: Ultraviolet to Gamma Ray. SPIE, Bellingham, p. 106996M
Magdziarz P., Zdziarski A. A., 1995, MNRAS, 273, 837
Makishima K. et al., 2000, ApJ, 535, 632
Malkan M. A., Sargent W. L. W., 1982, ApJ, 254, 22
Markoff S., Falcke H., Fender R., 2001, A&A, 372, L25
Mason R. E. et al., 2012, AJ, 144, 11
Matt G., Perola G. C., Piro L., 1991, A&A, 247, 25
McHardy I. M., Gunn K. F., Uttley P., Goad M. R., 2005, MNRAS, 359, 1469
Mehdipour M. et al., 2011, A&A, 534, A39
Merloni A., Heinz S., di Matteo T., 2003, MNRAS, 345, 1057
Middei R., Bianchi S., Marinucci A., Matt G., Petrucci P. O., Tamborra F., Tortosa A., 2019, A&A, 630, A131
Molina M. et al., 2009, MNRAS, 399, 1293
Molina M., Bassani L., Malizia A., Stephen J. B., Bird A. J., Bazzano A., Ubertini P., 2013, MNRAS, 433, 1687
Nagar N. M., Falcke H., Wilson A. S., 2005, A&A, 435, 521
Nandi P., Chatterjee A., Chakrabarti S. K., Dutta B. G., 2021, MNRAS, 506, 3111

Narayan R., Yi I., 1994, ApJ, 428, L13
Narayan R., Mahadevan R., Grindlay J. E., Popham R. G., Gammie C., 1998, ApJ, 492, 554
Nemmen R. S., Storchi-Bergmann T., Eracleous M., 2014, MNRAS, 438, 2804
Oh K. et al., 2018, ApJS, 235, 4
Pal I., Stalin C. S., Mallick L., Rani P., 2022, A&A 662, 78
Panessa F. et al., 2011, MNRAS, 417, 2426
Perola G. C., Matt G., Cappi M., Fiore F., Guainazzi M., Maraschi L., Petrucci P. O., Piro L., 2002, A&A, 389, 802
Petrucci P. O. et al., 2001, ApJ, 556, 716
Plotkin R. M., Gallo E., Jonker P. G., 2013, ApJ, 773, 59
Pozdnyakov L. A., Sobol I. M., Syunyaev R. A., 1983, Astrophys. Space Phys. Res., 2, 189
Ptak A., Terashima Y., Ho L. C., Quataert E., 2004, ApJ, 606, 173
Qiao E., Liu B. F., 2013, ApJ, 764, 2
Quataert E., 2001, in Peterson B. M., Pogge R. W., Polidan R. S., eds, ASP Conf. Ser. Vol. 224, Probing the Physics of Active Galactic Nuclei. Astron. Soc. Pac., San Francisco, p.71
Rani P., Stalin C. S., Goswami K. D., 2019, MNRAS, 484, 5113
Rees M. J., 1984, ARA&A, 22, 471
Reis R. C., Miller J. M., 2013, ApJ, 769, L7
Ricci C., Paltani S., Awaki H., Petrucci P. O., Ueda Y., Brightman M., 2013, A&A, 553, A29
Ricci C., Ueda Y., Koss M. J., Trakhtenbrot B., Bauer F. E., Gandhi P., 2015, ApJ, 815, L13
Ricci C. et al., 2017a, ApJS, 233, 17
Ricci C. et al., 2017b, Nature, 549, 488
Ricci C. et al., 2018, MNRAS, 480, 1819
Ricci C. et al., 2022, ApJ, 938, 67
Risaliti G., Young M., Elvis M., 2009, ApJ, 700, L6
Risaliti G., Nardini E., Salvati M., Elvis M., Fabbiano G., Maiolino R., Pietrini P., Torricelli-Ciamponi G., 2011, MNRAS, 410, 1027
Rybicki G. B., Lightman A. P., 1979, Radiative Processes in Astrophysics, Wiley-Interscience Publication, New York
Shakura N. I., Sunyaev R. A., 1973, A&A, 500, 33
She R., Ho L. C., Feng H., Cui C., 2018, ApJ, 859, 152
Shemmer O., Brandt W. N., Netzer H., Maiolino R., Kaspi S., 2006, ApJ, 646, L29
Shemmer O., Brandt W. N., Netzer H., Maiolino R., Kaspi S., 2008, ApJ, 682, 81
Singh K. P., Garmire G. P., Nousek J., 1985, ApJ, 297, 633
Stern B. E., Poutanen J., Svensson R., Sikora M., Begelman M. C., 1995, ApJ, 449, L13
Sunyaev R. A., Titarchuk L. G., 1980, A&A, 500, 167
Sunyaev R. A., Titarchuk L. G., 1985, A&A, 143, 374
Svensson R., 1982a, ApJ, 258, 321
Svensson R., 1982b, ApJ, 258, 335
Svensson R., 1984, MNRAS, 209, 175
Titarchuk L., 1994, ApJ, 434, 570
Tortosa A., Bianchi S., Marinucci A., Matt G., Petrucci P. O., 2018, A&A, 614, A37
Trakhtenbrot B. et al., 2017, MNRAS, 470, 800
Treister E., Krolik J. H., Dullemond C., 2008, ApJ, 679, 140
Tully R. B., 1988, Nearby Galaxies Catalog, Cambridge University Press, Cambridge
U V. et al., 2013, ApJ, 775, 115
Ueda Y., Akiyama M., Ohta K., Miyaji T., 2003, ApJ, 598, 886
Ueda Y., Akiyama M., Hasinger G., Miyaji T., Watson M. G., 2014, ApJ, 786, 104
Uttley P., Cackett E. M., Fabian A. C., Kara E., Wilkins D. R., 2014, A&AR, 22, 72
Vasudevan R. V., Fabian A. C., 2009, MNRAS, 392, 1124
Verner D. A., Ferland G. J., Korista K. T., Yakovlev D. G., 1996, ApJ, 465, 487
Weisskopf M. C. et al., 2016, in den Herder J.-W. A., Takahashi T., Bautz M., eds, Proc. SPIE Conf. Ser. Vol. 9905, Space Telescopes and Instrumentation 2016: Ultraviolet to Gamma Ray. SPIE, Bellingham, p. 990517
Woo J.-H., Urry C. M., 2002, ApJ, 579, 530
Yang Q.-X., Xie F.-G., Yuan F., Zdziarski A. A., Gierliński M., Ho L. C., Yu Z., 2015, MNRAS, 447, 1692
Younes G., Porquet D., Sabra B., Reeves J. N., 2011, A&A, 530, A149
Younes G., Ptak A., Ho L. C., Xie F.-G., Terasima Y., Yuan F., Huppenkothen D., Yukita M., 2019, ApJ, 870, 73
Yuan F., Narayan R., 2014, ARA&A, 52, 529
Zdziarski A. A., 1985, ApJ, 289, 514
Zdziarski A. A., Johnson W. N., Magdziarz P., 1996, MNRAS, 283, 193
Zdziarski A. A., Lubiński P., Smith D. A., 1999, MNRAS, 303, L11
Zoghbi A., Fabian A. C., Reynolds C. S., Cackett E. M., 2012, MNRAS, 422, 129

APPENDIX A: SPECTRAL VARIABILITY FOR NON-SIMULTANEOUS DATA

We used *XMM–Newton* observations for 12 sources in our sample. Five of these 12 *XMM–Newton* observations were not made simultaneously with the *NuSTAR*. We checked if there is any spectral variability between the *XMM–Newton* and *NuSTAR* data for non-simultaneous observations. We performed joint fitting of *XMM–Newton* and *NuSTAR* data in common energy range, i.e. in 3–10 keV range to check the variability. We used simple absorbed power-law model, along with a Gaussian component, for the Fe K-line. We allowed Γ and power-law normalization vary freely between two data sets. We find that Γ does not vary more than 10 per cent between the *XMM–Newton*, and *NuSTAR* observations for each of the five objects, while power-law normalization changes. The change in the power-law normalization can be taken care of by using 'cross-normalization' factor. As Γ did not vary more than 10 per cent, we used *XMM–Newton* data with the *NuSTAR* data for non-simultaneous observations.

Similar to the non-simultaneous *XMM–Newton* data, we also checked for spectral variability while adding the time-integrated BAT spectra with the *NuSTAR* spectra. We fitted the joint *NuSTAR* + BAT data in the common energy range (i.e. 15–78 keV) with a cutoff power-law model. The spectral parameters (Γ and $E_{\rm cut}$) are found to be consistent (within 10 per cent) for both *NuSTAR* and BAT spectra in the 15–78 keV energy range.

APPENDIX B: ADDITION OF TIME-INTEGRATED BAT SPECTRA

We used 105-months BAT data for the spectra analysis. The BAT spectra were added with the *NuSTAR* and *XMM–Newton* or XRT data, which were obtained in short time-scale ($\sim$10 to $-$100 ks). For individual sources, there is a possibility that the spectral state of AGN could change in the BAT time-scale, so it may not be appropriate to add BAT spectra with the pointed observations of *NuSTAR* and *XMM–Newton*. However, as the current work focus on the statistical properties of LAC-AGNs, the addition of time-integrated BAT data do not change the overall findings. We checked that if spectral analysis with and without the BAT spectra and the correlation properties of various spectral parameters remains the same. The addition of the BAT data allow us to probe the spectra up to 150 keV which it improves the uncertainty of the spectral parameters.

APPENDIX C: SPECTRAL ANALYSIS RESULT

Table C1. Spectral analysis result with Model-1a and Model-1b.

Object	Model-1a					Model-1b				
	$\log N_{\rm H}^{\rm los}$ $\log(\rm cm^{-2})$	Γ	$E_{\rm cut}$ (keV)	R	χ^2/dof	$\log N_{\rm H}^{\rm los}$ $\log(\rm cm^{-2})$	Γ	$kT_{\rm e}$ (keV)	R	χ^2/dof
(1)	(2)	(3)	(4)	(5)	(6)	(7)	(8)	(9)	(10)	(11)
NGC 454E	$23.58^{+0.06}_{-0.09}$	$1.80^{+0.07}_{-0.05}$	>352	>0.91	231/207	$23.58^{+0.06}_{-0.09}$	$1.78^{+0.05}_{-0.08}$	>165	>0.94	236/209
NGC 1052	$23.16^{+0.03}_{-0.04}$	$1.71^{+0.04}_{-0.06}$	254^{+152}_{-113}	>1.33	939/968	$23.17^{+0.03}_{-0.05}$	$1.70^{+0.05}_{-0.04}$	87^{+42}_{-39}	>1.44	819/890
NGC 2110	$22.59^{+0.02}_{-0.01}$	$1.68^{+0.05}_{-0.04}$	218^{+35}_{-47}	<0.04	2356/2226	$22.58^{+0.02}_{-0.02}$	$1.69^{+0.05}_{-0.06}$	73^{+32}_{-15}	<0.07	2365/2226
NGC 2655	$23.23^{+0.37}_{-0.16}$	$1.51^{+0.06}_{-0.08}$	>44	>0.48	116/122	$23.22^{+0.26}_{-0.14}$	$1.50^{+0.06}_{-0.09}$	>23	>0.49	119/122
NGC 3079	$24.24^{+0.12}_{-0.07}$	$1.81^{+0.05}_{-0.09}$	164^{+82}_{-58}	>1.45	274/296	$24.24^{+0.13}_{-0.08}$	$1.81^{+0.05}_{-0.08}$	52^{+22}_{-12}	>1.44	275/296
NGC 3147	$22.09^{+0.06}_{-0.06}$	$1.90^{+0.04}_{-0.06}$	395^{+167}_{-44}	$0.41^{+0.34}_{-0.22}$	621/579	$22.09^{+0.06}_{-0.07}$	$1.91^{+0.04}_{-0.05}$	156^{+74}_{-31}	$0.41^{+0.35}_{-0.45}$	619/579
NGC 3718	$21.94^{+0.05}_{-0.04}$	$1.84^{+0.04}_{-0.06}$	267^{+117}_{-81}	<0.18	1282/1238	$21.95^{+0.03}_{-0.03}$	$1.83^{+0.03}_{-0.04}$	115^{+60}_{-42}	<0.16	1285/1238
NGC 3786	$21.83^{+0.26}_{-0.09}$	$1.64^{+0.05}_{-0.08}$	186^{+102}_{-75}	$1.04^{+0.57}_{-0.24}$	182/185	$21.83^{+0.31}_{-0.13}$	$1.71^{+0.05}_{-0.06}$	81^{+38}_{-22}	$1.03^{+0.56}_{-0.39}$	181/185
NGC 3998	20.00*	$1.86^{+0.08}_{-0.05}$	252^{+117}_{-82}	<0.01	1512/1565	20.00*	$1.86^{+0.05}_{-0.04}$	102^{+54}_{-16}	<0.01	1519/1565
NGC 4102	$23.85^{+0.10}_{-0.09}$	$1.68^{+0.05}_{-0.07}$	201^{+72}_{-43}	>0.44	401/361	$23.86^{+0.09}_{-0.08}$	$1.67^{+0.06}_{-0.06}$	72^{+43}_{-2}	>0.45	399/361
NGC 4258	$23.00^{+0.10}_{-0.06}$	$1.77^{+0.05}_{-0.07}$	391^{+167}_{-121}	<0.15	792/884	$23.00^{+0.09}_{-0.06}$	$1.78^{+0.05}_{-0.06}$	149^{+82}_{-43}	<0.19	866/884
NGC 4579	20.00*	$1.96^{+0.06}_{-0.05}$	458^{+122}_{-95}	<0.01	1647/1663	20.00*	$1.96^{+0.06}_{-0.04}$	195^{+91}_{-63}	<0.01	1649/1663
NGC 5033	$21.67^{+0.18}_{-0.13}$	$1.76^{+0.05}_{-0.08}$	201^{+168}_{-61}	<0.18	1364/1379	$21.71^{+0.20}_{-0.09}$	$1.76^{+0.04}_{-0.08}$	68^{+18}_{-19}	<0.19	1369/1369
NGC 5283	$23.10^{+0.02}_{-0.03}$	$1.77^{+0.05}_{-0.08}$	91^{+23}_{-21}	$0.69^{+0.42}_{-0.12}$	428/425	$23.10^{+0.02}_{-0.03}$	$1.78^{+0.05}_{-0.07}$	45^{+13}_{-0}	$0.71^{+0.45}_{-0.19}$	428/423
NGC 5290	$22.12^{+0.08}_{-0.09}$	$1.76^{+0.04}_{-0.07}$	260^{+103}_{-88}	$0.57^{+0.38}_{-0.43}$	515/603	$22.13^{+0.14}_{-0.09}$	$1.76^{+0.05}_{-0.08}$	104^{+61}_{-15}	$0.60^{+0.34}_{-0.38}$	522/608
NGC 5899	$22.94^{+0.07}_{-0.07}$	$1.74^{+0.06}_{-0.10}$	115^{+43}_{-25}	<0.52	326/396	$22.94^{+0.06}_{-0.07}$	$1.74^{+0.05}_{-0.08}$	45^{+22}_{-12}	<0.59	334/396
NGC 6232	$23.53^{+0.32}_{-0.16}$	$1.44^{+0.06}_{-0.10}$	>55	>0.68	143/141	$23.53^{+0.30}_{-0.14}$	$1.43^{+0.04}_{-0.10}$	>21	>0.71	145/141
NGC 7213	$21.81^{+0.12}_{-0.07}$	$1.87^{+0.03}_{-0.05}$	266^{+217}_{-56}	<0.05	1204/1201	$21.81^{+0.14}_{-0.06}$	$1.87^{+0.05}_{-0.08}$	111^{+103}_{-32}	<0.07	1199/1201
NGC 7674	$23.61^{+0.23}_{-0.11}$	$1.64^{+0.04}_{-0.09}$	>47	>0.74	114/106	$23.61^{+0.26}_{-0.11}$	$1.62^{+0.05}_{-0.09}$	>20	>0.69	118/106
Mrk 18	$23.16^{+0.10}_{-0.10}$	$1.74^{+0.09}_{-0.10}$	>277	>0.66	76/73	$23.15^{+0.10}_{-0.09}$	$1.75^{+0.08}_{-0.04}$	>88	>0.64	76/73
Mrk 273	$23.43^{+0.06}_{-0.03}$	$1.70^{+0.05}_{-0.09}$	>238	>0.71	499/442	$23.43^{+0.06}_{-0.04}$	$1.69^{+0.06}_{-0.09}$	>135	>0.70	502/442
ARP 102B	$21.73^{+0.39}_{-0.14}$	$1.72^{+0.05}_{-0.09}$	88^{+25}_{-28}	>0.84	259/281	$21.74^{+0.41}_{-0.16}$	$1.72^{+0.06}_{-0.09}$	35^{+22}_{-10}	>0.77	256/284
ESO 253–003	$23.04^{+0.11}_{-0.14}$	$1.41^{+0.05}_{-0.09}$	367^{+108}_{-174}	$0.85^{+0.35}_{-0.22}$	378/327	$23.04^{+0.13}_{-0.15}$	$1.42^{+0.05}_{-0.08}$	138^{+100}_{-41}	$0.86^{+0.41}_{-0.29}$	383/327
ESO 506–027	$23.80^{+0.07}_{-0.04}$	$1.67^{+0.05}_{-0.08}$	330^{+156}_{-175}	$0.86^{+0.41}_{-0.27}$	385/342	$23.80^{+0.07}_{-0.05}$	$1.67^{+0.06}_{-0.04}$	125^{+76}_{-42}	$0.85^{+0.45}_{-0.23}$	379/342
HE 1136–2304	$21.08^{+0.08}_{-0.12}$	$1.65^{+0.05}_{-0.09}$	231^{+75}_{-45}	<0.15	2768/2559	$21.08^{+0.08}_{-0.07}$	$1.65^{+0.03}_{-0.04}$	101^{+45}_{-21}	<0.13	2774/2559
IC 4518A	$23.21^{+0.11}_{-0.06}$	$1.54^{+0.06}_{-0.06}$	>41	>0.77	199/208	$23.21^{+0.11}_{-0.07}$	$1.55^{+0.06}_{-0.07}$	>19	>0.81	198/208
IGR J11366	$21.86^{+0.06}_{-0.07}$	$1.95^{+0.04}_{-0.05}$	126^{+35}_{-22}	$0.42^{+0.41}_{-0.34}$	495/516	$21.89^{+0.05}_{-0.08}$	$1.96^{+0.08}_{-0.06}$	59^{+76}_{-15}	$0.45^{+0.39}_{-0.34}$	502/516
UGC 12292	$24.20^{+0.10}_{-0.04}$	$1.67^{+0.06}_{-0.09}$	>62	>0.64	135/122	$24.19^{+0.10}_{-0.05}$	$1.67^{+0.05}_{-0.09}$	>40	>0.67	142/122
LEDA 214543	$22.40^{+0.12}_{-0.07}$	$1.72^{+0.03}_{-0.05}$	98^{+45}_{-33}	>0.77	465/545	$22.40^{+0.14}_{-0.08}$	$1.72^{+0.03}_{-0.06}$	39^{+19}_{-11}	>0.72	472/545
Z367–9	$23.26^{+0.07}_{-0.04}$	$1.84^{+0.05}_{-0.05}$	170^{+108}_{-71}	>0.64	234/229	$23.26^{+0.08}_{-0.06}$	$1.84^{+0.05}_{-0.08}$	52^{+38}_{-21}	>0.63	235/229

Notes. Columns: (1) Source Name, (2) logarithm of line of sight of column density ($N_{\rm H}^{\rm los}$), (3) photon index (Γ), (4) cut-off energy ($E_{\rm cut}$) in keV, (5) reflection fraction (R), (6) χ^2/degrees of freedom for Model-1a, (7) logarithm of line of sight of column density ($N_{\rm H}^{\rm los}$), (8) photon index (Γ), (9) hot electron plasma temperature ($kT_{\rm e}$) in keV, (10) reflection fraction (R), (11) χ^2/degrees of freedom for Model-2. Columns (2–5) represent the spectral parameters obtained from Model-1a, while columns (6–10) represent the results obtained with Model-1b.

Table C2. Spectral analysis result with Model-2a and Model-2b.

	Model-2a					Model-2b				
Object	$\log N_{\rm H}^{\rm los}$ $\log(\rm cm^{-2})$	$\log N_{\rm H}^{\rm tor}$ $\log(\rm cm^{-2})$	Γ	$E_{\rm cut}$ (keV)	χ^2/dof	$\log N_{\rm H}^{\rm los}$ $\log(\rm cm^{-2})$	$\log N_{\rm H}^{\rm tor}$ $\log(\rm cm^{-2})$	Γ	$kT_{\rm e}$ (keV)	χ^2/dof
(1)	(2)	(3)	(4)	(5)	(6)	(7)	(8)	(9)	(10)	(11)
NGC 454E	$23.61^{+0.03}_{-0.03}$	$24.54^{+0.91}_{-1.35}$	$1.77^{+0.05}_{-0.05}$	>287	233/207	$23.61^{+0.03}_{-0.03}$	$24.52^{+0.95}_{-1.26}$	$1.77^{+0.03}_{-0.01}$	>111	235/209
NGC 1052	$23.17^{+0.03}_{-0.03}$	$23.87^{+0.22}_{-0.25}$	$1.73^{+0.02}_{-0.03}$	267^{+148}_{-125}	936/968	$23.17^{+0.03}_{-0.04}$	$23.80^{+0.28}_{-0.21}$	$1.72^{+0.02}_{-0.02}$	91^{+45}_{-33}	814/890
NGC 2110	$22.59^{+0.01}_{-0.02}$	$22.66^{+0.16}_{-0.31}$	$1.66^{+0.01}_{-0.01}$	229^{+28}_{-28}	2292/2226	$22.60^{+0.02}_{-0.01}$	$22.66^{+0.26}_{-0.52}$	$1.74^{+0.01}_{-0.01}$	89^{+15}_{-10}	2320/2226
NGC 2655	$23.23^{+0.39}_{-0.14}$	$23.59^{+0.56}_{-0.81}$	$1.52^{+0.05}_{-0.03}$	>49	110/122	$23.23^{+0.37}_{-0.13}$	$23.59^{+0.62}_{-0.86}$	$1.53^{+0.04}_{-0.05}$	>19	113/122
NGC 3079	$24.26^{+0.08}_{-0.06}$	$24.64^{+0.35}_{-0.16}$	$1.84^{+0.03}_{-0.04}$	110^{+52}_{-29}	262/296	$24.27^{+0.09}_{-0.06}$	$24.62^{+0.34}_{-0.21}$	$1.85^{+0.06}_{-0.04}$	39^{+17}_{-10}	268/297
NGC 3147	$22.09^{+0.06}_{-0.05}$	$24.75^{+1.74}_{-0.88}$	$1.90^{+0.04}_{-0.04}$	410^{+152}_{-38}	612/579	$22.11^{+0.06}_{-0.05}$	$24.76^{+1.81}_{-0.92}$	$1.92^{+0.06}_{-0.06}$	189^{+65}_{-29}	610/579
NGC 3718	$21.95^{+0.04}_{-0.04}$	$22.72^{+1.67}_{-0.72}$	$1.87^{+0.02}_{-0.02}$	296^{+105}_{-74}	1261/1238	$21.96^{+0.03}_{-0.03}$	$22.78^{+1.54}_{-0.87}$	$1.89^{+0.01}_{-0.02}$	142^{+65}_{-48}	1276/1238
NGC 3786	$21.84^{+0.24}_{-0.07}$	$24.71^{+0.68}_{-0.81}$	$1.73^{+0.03}_{-0.04}$	192^{+109}_{-82}	164/185	$21.83^{+0.20}_{-0.09}$	$24.72^{+0.74}_{-0.47}$	$1.73^{+0.04}_{-0.03}$	92^{+45}_{-35}	165/185
NGC 3998	20.00*	$22.91^{+0.24}_{-0.18}$	$1.90^{+0.04}_{-0.03}$	276^{+143}_{-66}	1493/1565	20.00*	$22.90^{+0.28}_{-0.19}$	$1.90^{+0.02}_{-0.02}$	132^{+92}_{-21}	1496/1565
NGC 4102	$23.85^{+0.09}_{-0.08}$	$25.51^{+25.00}_{-0.64}$	$1.70^{+0.03}_{-0.03}$	206^{+74}_{-45}	397/361	$23.86^{+0.08}_{-0.08}$	$25.51^{+25.00}_{-0.76}$	$1.69^{+0.01}_{-0.03}$	74^{+53}_{-9}	396/261
NGC 4258	$23.00^{+0.08}_{-0.06}$	$23.54^{+0.45}_{-0.71}$	$1.81^{+0.02}_{-0.02}$	448^{+158}_{-128}	779/884	$23.00^{+0.08}_{-0.06}$	$23.56^{+0.52}_{-0.73}$	$1.82^{+0.04}_{-0.03}$	197^{+66}_{-45}	856/884
NGC 4579	20.00*	$23.80^{+0.17}_{-0.12}$	$1.96^{+0.04}_{-0.05}$	410^{+131}_{-77}	1646/1663	20.00*	$23.78^{+0.12}_{-0.15}$	$1.98^{+0.03}_{-0.02}$	190^{+88}_{-58}	1649/1663
NGC 5033	$21.68^{+0.16}_{-0.10}$	$23.80^{+0.09}_{-0.09}$	$1.78^{+0.03}_{-0.03}$	208^{+175}_{-66}	1363/1379	$21.72^{+0.13}_{-0.09}$	$23.80^{+0.10}_{-0.07}$	$1.82^{+0.02}_{-0.02}$	71^{+15}_{-21}	1365/1379
NGC 5283	$23.10^{+0.03}_{-0.03}$	$24.18^{+0.58}_{-0.34}$	$1.79^{+0.03}_{-0.04}$	82^{+24}_{-15}	422/425	$23.10^{+0.03}_{-0.03}$	$24.20^{+0.66}_{-0.45}$	$1.82^{+0.04}_{-0.04}$	39^{+14}_{-8}	423/423
NGC 5290	$22.13^{+0.08}_{-0.08}$	$24.02^{+0.54}_{-0.68}$	$1.75^{+0.03}_{-0.04}$	247^{+109}_{-92}	512/603	$22.14^{+0.12}_{-0.08}$	$24.04^{+0.59}_{-0.78}$	$1.75^{+0.04}_{-0.03}$	107^{+56}_{-18}	493/608
NGC 5899	$22.95^{+0.07}_{-0.07}$	$24.89^{+25.00}_{-0.49}$	$1.76^{+0.04}_{-0.03}$	122^{+35}_{-22}	306/396	$22.94^{+0.07}_{-0.07}$	$24.91^{+25.00}_{-0.45}$	$1.76^{+0.03}_{-0.04}$	48^{+15}_{-10}	308/396
NGC 6232	$23.57^{+0.32}_{-0.15}$	$25.15^{+25.00}_{-0.51}$	$1.46^{+0.05}_{-0.04}$	>48	144/141	$23.57^{+0.32}_{-0.15}$	$25.14^{+25.00}_{-0.59}$	$1.45^{+0.04}_{-0.04}$	>21	146/141
NGC 7213	$21.81^{+0.14}_{-0.08}$	$23.45^{+0.14}_{-0.18}$	$1.91^{+0.06}_{-0.05}$	312^{+262}_{-48}	1215/1201	$21.82^{+0.13}_{-0.07}$	$23.46^{+0.16}_{-0.22}$	$1.90^{+0.10}_{-0.10}$	146^{+165}_{-16}	1188/1201
NGC 7674	$23.61^{+0.25}_{-0.10}$	$24.57^{+25.50}_{-1.02}$	$1.62^{+0.06}_{-0.09}$	>37	115/106	$23.61^{+0.28}_{-0.11}$	$24.56^{+25.00}_{-0.94}$	$1.61^{+0.09}_{-0.08}$	>18	120/106
Mrk 18	$23.16^{+0.10}_{-0.09}$	$25.01^{+25.00}_{-2.73}$	$1.79^{+0.04}_{-0.03}$	>320	79/73	$23.15^{+0.09}_{-0.08}$	$25.51^{+25.00}_{-2.67}$	$1.78^{+0.08}_{-0.05}$	>88	81/73
Mrk 273	$23.43^{+0.05}_{-0.04}$	$24.26^{+0.82}_{-0.46}$	$1.71^{+0.03}_{-0.05}$	>252	502/442	$23.43^{+0.05}_{-0.04}$	$24.42^{+0.78}_{-0.52}$	$1.71^{+0.03}_{-0.02}$	>142	500/442
ARP 102B	$21.75^{+0.47}_{-0.16}$	$24.69^{+0.68}_{-0.54}$	$1.75^{+0.04}_{-0.03}$	84^{+22}_{-14}	251/281	$21.77^{+0.59}_{-0.12}$	$24.65^{+0.76}_{-0.58}$	$1.76^{+0.04}_{-0.06}$	31^{+13}_{-9}	252/284
ESO 253–003	$23.04^{+0.10}_{-0.15}$	$24.06^{+0.35}_{-0.25}$	$1.44^{+0.04}_{-0.04}$	386^{+112}_{-205}	381/327	$23.04^{+0.10}_{-0.17}$	$24.08^{+0.29}_{-0.24}$	$1.45^{+0.05}_{-0.04}$	148^{+106}_{-37}	388/342
ESO 506–027	$23.80^{+0.07}_{-0.04}$	$24.15^{+0.65}_{-0.41}$	$1.69^{+0.04}_{-0.02}$	363^{+138}_{-159}	386/342	$23.80^{+0.07}_{-0.05}$	$24.12^{+0.75}_{-0.56}$	$1.69^{+0.04}_{-0.05}$	138^{+78}_{-56}	384/342
HE 1136–2304	$21.08^{+0.08}_{-0.03}$	$23.15^{+0.15}_{-0.12}$	$1.67^{+0.09}_{-0.09}$	256^{+92}_{-52}	2754/2559	$21.11^{+0.07}_{-0.06}$	$23.20^{+0.21}_{-0.17}$	$1.67^{+0.05}_{-0.03}$	116^{+44}_{-38}	2752/2559
IC 4518A	$23.21^{+0.10}_{-0.07}$	$24.76^{+0.53}_{-0.30}$	$1.55^{+0.04}_{-0.09}$	>35	198/208	$23.20^{+0.12}_{-0.07}$	$24.73^{+0.65}_{-0.45}$	$1.56^{+0.04}_{-0.05}$	>15	195/208
IGR J11366	$21.88^{+0.07}_{-0.04}$	$24.30^{+0.32}_{-0.25}$	$1.94^{+0.06}_{-0.06}$	109^{+32}_{-19}	487/516	$21.89^{+0.06}_{-0.04}$	$24.27^{+0.36}_{-0.24}$	$1.96^{+0.06}_{-0.06}$	58^{+80}_{-13}	495/516
UGC 12282	$24.20^{+0.08}_{-0.05}$	$24.82^{+0.45}_{-0.59}$	$1.69^{+0.04}_{-0.06}$	>57	137/122	$24.21^{+0.10}_{-0.06}$	$24.83^{+0.75}_{-0.85}$	$1.68^{+0.03}_{-0.05}$	>39	144/122
LEDA214543	$22.39^{+0.10}_{-0.07}$	$24.56^{+0.45}_{-0.36}$	$1.71^{+0.02}_{-0.04}$	106^{+52}_{-29}	452/545	$22.39^{+0.10}_{-0.07}$	$24.56^{+0.48}_{-0.35}$	$1.71^{+0.05}_{-0.05}$	36^{+21}_{-10}	467/545
Z367–9	$23.27^{+0.07}_{-0.04}$	$24.10^{+0.72}_{-0.46}$	$1.86^{+0.03}_{-0.02}$	175^{+114}_{-79}	232/229	$23.27^{+0.08}_{-0.05}$	$24.05^{+0.68}_{-0.52}$	$1.88^{+0.04}_{-0.05}$	56^{+41}_{-25}	233/229

Notes. * fixed during analysis.

Columns: (1) Source name, (2) logarithm of line of sight of column density ($N_{\rm H}^{\rm los}$), (3) logarithm of average column density of the obscuring materials ($N_{\rm H}^{\rm tor}$), (4) photon index (Γ), (5) cut-off energy ($E_{\rm cut}$) in keV, (6) χ^2/degrees of freedom for Model-2a, (7) logarithm of line of sight of column density ($N_{\rm H}^{\rm los}$), (8) logarithm of average column density of the obscuring materials ($N_{\rm H}^{\rm tor}$), (9) photon index (Γ), (10) hot electron plasma temperature of the corona ($kT_{\rm e}$) in keV, (11) χ^2/degrees of freedom for Model-2b. Columns (2–5) represent the spectral parameters obtained from Model-2a, while columns (6–10) represent the results obtained with Model-2b.

Table C3. Important parameters.

Object	$\log L_{\rm bol}$ $\log\,(\rm erg\ s^{-1})$	$\log \lambda_{\rm Edd}$	θ	$\tau_{\rm e}$	l	$N_{\rm S}$	$\log L_{\rm jet}$ $\log\ (\rm erg\ s^{-1})$
(1)	(2)	(3)	(4)	(5)	(6)	(7)	
NGC 454E	43.05 ± 0.02	-3.584 ± 0.472	>0.23	<1.33	$0.60^{+1.17}_{-0.40}$	>2	44.23 ± 0.03
NGC 1052	42.63 ± 0.01	-4.444 ± 0.304	$0.18^{+0.09}_{-0.06}$	$1.42^{+0.41}_{-0.61}$	$0.08^{+0.08}_{-0.04}$	6^{+2}_{-2}	44.78 ± 0.08
NGC 2110	43.37 ± 0.02	-4.124 ± 0.121	$0.17^{+0.03}_{-0.02}$	$1.41^{+0.17}_{-0.15}$	$0.17^{+0.05}_{-0.04}$	6^{+1}_{-1}	44.66 ± 0.04
NGC 2655	41.97 ± 0.01	-3.844 ± 0.208	>0.03	<7.72	$0.33^{+0.20}_{-0.13}$	>23	43.78 ± 0.03
NGC 3079	42.54 ± 0.02	-3.844 ± 0.321	$0.08^{+0.03}_{-0.02}$	$2.28^{+0.57}_{-0.63}$	$0.33^{+0.36}_{-0.17}$	9^{+2}_{-2}	44.37 ± 0.04
NGC 3147	42.68 ± 0.02	-4.224 ± 0.122	$0.37^{+0.13}_{-0.06}$	$0.62^{+0.16}_{-0.15}$	$0.14^{+0.04}_{-0.03}$	2^{+1}_{-1}	44.25 ± 0.03
NGC 3718	41.52 ± 0.02	-6.124 ± 0.122	$0.28^{+0.13}_{-0.09}$	$0.82^{+0.23}_{-0.35}$	$0.002^{+0.001}_{-0.001}$	3^{+3}_{-1}	42.40 ± 0.09
NGC 3786	42.18 ± 0.02	-3.464 ± 0.118	$0.18^{+0.09}_{-0.07}$	$1.39^{+0.42}_{-0.66}$	$0.79^{+0.25}_{-0.19}$	6^{+3}_{-2}	43.55 ± 0.05
NGC 3998	42.30 ± 0.02	-5.744 ± 0.241	$0.26^{+0.14}_{-0.04}$	$0.86^{+0.28}_{-0.15}$	$0.004^{+0.003}_{-0.002}$	3^{+1}_{-2}	43.43 ± 0.05
NGC 4102	42.42 ± 0.01	-4.444 ± 0.344	$0.14^{+0.09}_{-0.02}$	$1.72^{+0.55}_{-0.24}$	$0.08^{+0.10}_{-0.04}$	7^{+1}_{-2}	43.67 ± 0.02
NGC 4258	41.39 ± 0.03	-4.294 ± 0.382	$0.39^{+0.13}_{-0.09}$	$0.68^{+0.17}_{-0.19}$	$0.12^{+0.16}_{-0.07}$	2^{+1}_{-1}	43.59 ± 0.03
NGC 4579	42.65 ± 0.02	-3.564 ± 0.121	$0.37^{+0.17}_{-0.11}$	$0.58^{+0.18}_{-0.23}$	$0.63^{+0.20}_{-0.15}$	2^{+1}_{-1}	43.75 ± 0.04
NGC 5033	42.15 ± 0.02	-3.824 ± 0.373	$0.14^{+0.03}_{-0.04}$	$1.52^{+0.24}_{-0.49}$	$0.35^{+0.46}_{-0.20}$	6^{+2}_{-1}	42.39 ± 0.05
NGC 5283	43.01 ± 0.01	-3.974 ± 0.311	$0.08^{+0.03}_{-0.02}$	$2.35^{+0.54}_{-0.51}$	$0.25^{+0.25}_{-0.13}$	9^{+2}_{-2}	43.48 ± 0.05
NGC 5290	42.83 ± 0.02	-3.044 ± 0.334	$0.21^{+0.11}_{-0.04}$	$1.21^{+0.39}_{-0.24}$	$2.09^{+2.37}_{-1.11}$	5^{+1}_{-2}	43.74 ± 0.04
NGC 5899	43.16 ± 0.02	-3.614 ± 0.334	$0.09^{+0.03}_{-0.02}$	$2.16^{+0.44}_{-0.50}$	$0.56^{+0.64}_{-0.30}$	9^{+2}_{-2}	43.78 ± 0.04
NGC 6232	42.48 ± 0.01	-3.064 ± 0.527	>0.04	<5.98	$1.99^{+4.76}_{-1.40}$	>23	44.33 ± 0.03
NGC 7213	43.06 ± 0.01	-3.044 ± 0.111	$0.29^{+0.24}_{-0.03}$	$0.79^{+0.36}_{-0.15}$	$2.09^{+0.60}_{-0.47}$	3^{+1}_{-2}	44.27 ± 0.06
NGC 7674	43.15 ± 0.04	-4.144 ± 0.141	>0.04	<6.02	$0.17^{+0.06}_{-0.05}$	>20	45.75 ± 0.03
Mrk 18	42.82 ± 0.02	-3.144 ± 0.318	>0.17	<1.98	$1.66^{+1.80}_{-0.86}$	>2	43.94 ± 0.04
Mrk 273	43.68 ± 0.02	-3.454 ± 0.062	>0.28	<1.11	$0.81^{+0.12}_{-0.11}$	>2	45.69 ± 0.03
ARP 102B	43.58 ± 0.02	-3.454 ± 0.363	$0.06^{+0.03}_{-0.02}$	$2.92^{+0.72}_{-0.98}$	$0.81^{+1.05}_{-0.45}$	12^{+4}_{-3}	45.28 ± 0.03
ESO 253–003	43.83 ± 0.02	-4.124 ± 0.124	$0.27^{+21}_{-0.05}$	$1.57^{+1.10}_{-0.42}$	$0.17^{+0.06}_{-0.04}$	8^{+2}_{-4}	46.44 ± 0.14
ESO 506–027	44.07 ± 0.02	-3.034 ± 0.314	$0.27^{+0.15}_{-0.11}$	$1.07^{+0.37}_{-0.63}$	$2.13^{+2.22}_{-1.09}$	4^{+3}_{-2}	45.02 ± 0.04
HE 1136–2304	44.25 ± 0.02	-3.254 ± 0.121	$0.23^{+0.09}_{-0.05}$	$1.26^{+0.33}_{-0.32}$	$1.29^{+0.41}_{-0.31}$	5^{+1}_{-1}	44.28 ± 0.04
IC 4518A	43.37 ± 0.02	-3.304 ± 0.125	>0.03	<6.67	$1.15^{+0.36}_{-0.28}$	>26	45.26 ± 0.10
IGR J11366–3602	43.42 ± 0.02	-3.484 ± 0.121	$0.11^{+0.16}_{-0.03}$	$1.53^{+0.81}_{-0.42}$	$0.76^{+0.24}_{-0.18}$	6^{+2}_{-3}	–
UGC 12282	42.65 ± 0.02	-5.264 ± 0.371	>0.08	<2.91	$0.02^{+0.01}_{-0.01}$	>12	43.89 ± 0.02
LEDA214543	44.31 ± 0.02	-3.634 ± 0.338	$0.07^{+0.04}_{-0.02}$	$2.79^{+0.88}_{-0.87}$	$0.54^{+0.64}_{-0.29}$	11^{+3}_{-4}	43.72 ± 0.05
Z367–9	43.56 ± 0.01	-4.374 ± 0.332	$0.11^{+0.08}_{-0.05}$	$1.70^{+0.63}_{-1.02}$	$0.10^{+0.11}_{-0.05}$	7^{+4}_{-2}	43.80 ± 0.10

Notes. Columns: (1) Source name, (2) logarithm of the bolometric luminosity, (3) logarithm of the Eddington ratio, (4) dimensionless temperature, (5) optical depth of the hot electron plasma, (6) compactness parameter, (7) number of scattering of the seed photons in the Compton cloud, (8) logarithm of the jet luminosity.

APPENDIX D: CORNER PLOT

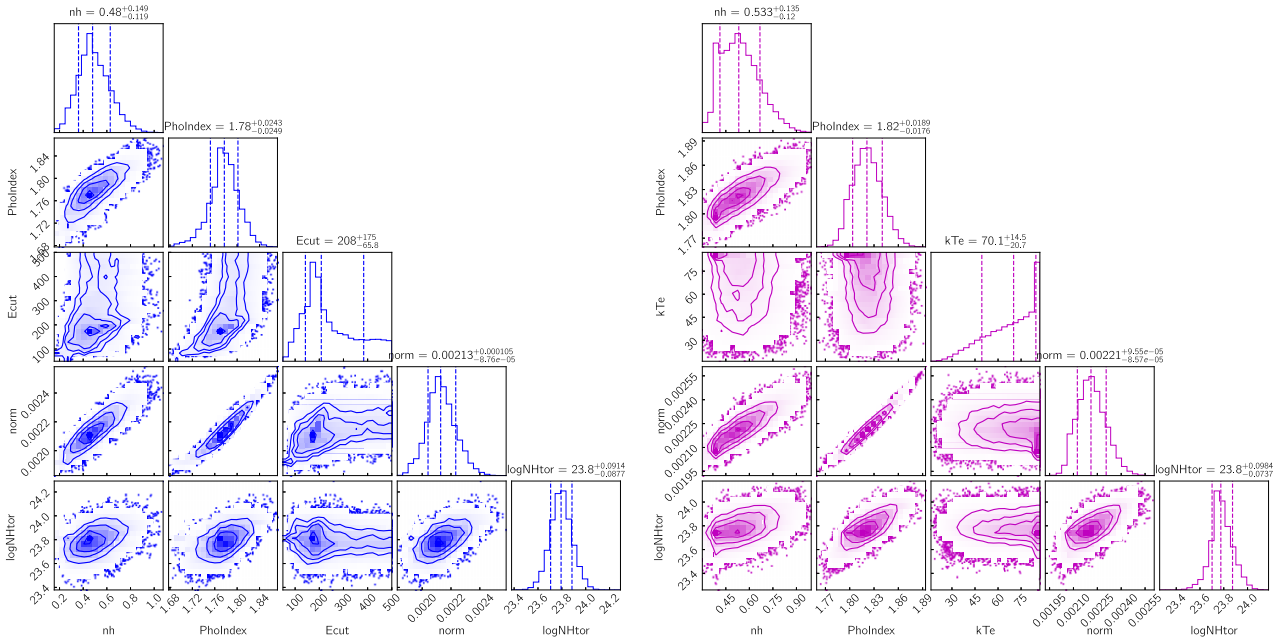

Figure D1. Posterior distribution of the spectral parameters obtained from the MCMC analysis with the Model-1 and Model-2, in the left-hand and right-hand panel, respectively. Plotting was performed using corner plot (Foreman-Mackey 2016). Central dashed lines correspond to the peak values whereas 1σ confidence levels are represented by dashed lines on either sides.

This paper has been typeset from a TEX/LATEX file prepared by the author.